Reprinted from MONTHLY WEATHER REVIEW, Vol. 118, No. 11, November 1990
American Meteorological Society

The 27–28 October 1986 FIRE IFO Cirrus Case Study: Cirrus Parameter Relationships Derived from Satellite and Lidar Data

PATRICK MINNIS*, DAVID F. YOUNG†, KENNETH SASSEN,**
JOSEPH M. ALVAREZ* AND CHRISTIAN J. GRUND‡

*Atmospheric Sciences Division, NASA Langley Research Center, Hampton, Virginia,
†Lockheed Engineering and Sciences Company, Hampton, Virginia,
**Department of Meteorology, University of Utah, Salt Lake City, Utah,
‡Department of Meteorology, University of Wisconsin, Madison, Wisconsin

(Manuscript received 24 March 1989, in final form 12 June 1990)

ABSTRACT

Cirrus cloud radiative and physical characteristics are determined using a combination of ground-based, aircraft, and satellite measurements taken as part of the FIRE Cirrus Intensive Field Observations (IFO) during October and November 1986. Lidar backscatter data are used with rawinsonde data to define cloud base, center, and top heights and the corresponding temperatures. Coincident GOES 4-km visible (0.65 μm) and 8-km infrared window (11.5 μm) radiances are analyzed to determine cloud emittances and reflectances. Infrared optical depth is computed from the emittance results. Visible optical depth is derived from reflectance using a theoretical ice crystal scattering model and an empirical bidirectional reflectance model. No clouds with visible optical depths greater than 5 or infrared optical depths less than 0.1 were used in the analysis.

Average cloud thickness ranged from 0.5 km to 8.0 km for the 71 scenes. Mean vertical beam emittances derived from cloud-center temperatures were 0.62 for all scenes compared to 0.33 for the case study (27–28 October) reflecting the thinner clouds observed for the latter scenes. Relationships between cloud emittance, extinction coefficients, and temperature for the case study are very similar to those derived from earlier surface-based studies. The thicker clouds seen during the other IFO days yield different results. Emittances derived using cloud-top temperature were ratioed to those determined from cloud-center temperature. A nearly linear relationship between these ratios and cloud-center temperature holds promise for determining actual cloud-top temperatures and cloud thicknesses from visible and infrared radiance pairs.

The mean ratio of the visible scattering optical depth to the infrared absorption optical depth was 2.13 for these data. This scattering efficiency ratio shows a significant dependence on cloud temperature. Values of mean scattering efficiency as high as 2.6 suggest the presence of small ice particles at temperatures below 230 K. The parameterization of visible reflectance in terms of cloud optical depth and clear-sky reflectance shows promise as a simplified method for interpreting visible satellite data reflected from cirrus clouds. Large uncertainties in the optical parameters due to cloud reflectance anisotropy and shading were found by analyzing data for various solar zenith angles and for simultaneous AVHRR data. Inhomogeneities in the cloud fields result in uneven cloud shading that apparently causes the occurrence of anomalously dark, cloudy pixels in the GOES data. These shading effects complicate the interpretation of the satellite data. The results highlight the need for additional study of cirrus cloud scattering processes and remote sensing techniques.

1. Introduction

Accurate quantification of cirrus cloud properties from satellite measurements is particularly important to the understanding of the role of cirrus in climate change. The nonblackness of cirrus at thermal infrared wavelengths renders the interpretation of satellite data taken over cirrus more difficult than measurements over most water clouds. The International Satellite Cloud Climatology Project (ISCCP; see Schiffer and Rossow 1983) is making an ambitious effort to derive daytime cirrus coverage, altitudes, and optical depths over the globe during a 5-year period. The ISCCP analysis algorithm (Rossow et al. 1988) relies entirely on bispectral data taken at visible (VIS: ~0.65 μm) and infrared (IR: ~11.5 μm) wavelengths. Although VIS–IR bispectral techniques have been suggested as feasible methods for determining bulk cirrus properties (e.g., Shenk and Curran 1973; Reynolds and Vonder Haar 1977), there has been very little application of these techniques to real data prior to the ISCCP.

The basic premise for using the bispectral approach is that the VIS extinction coefficient is related to the IR absorption coefficient. This relationship implies that the cloud VIS reflectance may be used to infer the cloud's IR emittance. Having a value for the clear-sky IR radiance, it is possible to correct the observed cloudy radiance for cloud emittance resulting in an estimate

Corresponding author address: Patrick Minnis, Atmospheric Sciences Division, NASA/Langley Research Center, Hampton, VA 23665-5225.

of the radiance emanating from a specified level in the cloud. The equivalent blackbody temperature of this level, usually the cloud center, is then converted to cloud altitude using a vertical sounding of temperature. The critical relationship required for this approach is the dependence of IR emittance on VIS reflectance through the IR and VIS optical depths. Since clouds scatter radiation anisotropically, this relationship is also influenced by the viewing and illumination conditions.

The ISCCP cirrus analysis (Rossow et al. 1988) utilizes a combination of theoretical and empirical models to determine the cloud visible optical depth from the observed reflectance; the cloud emittance from the visible optical depth; and finally, the cloud-top temperature from the cloud emittance and the observed infrared radiance. The theoretical cloud model is a radiative transfer scheme that simulates the scattering and absorption of visible radiation by water droplets with an effective radius of 10 μm. For water droplets of this size, the ratio of VIS extinction to infrared absorption optical depths is ~2.4. An analysis of coincident satellite and lidar data by Platt et al. (1980) and theoretical calculations employing cylinders (Platt 1979) suggest that this ratio is approximately equal to 2.0 for cirrus. The ISCCP algorithm utilizes the latter value to provide a link between the water droplet model and actual cirrus clouds.

Cirrus clouds are primarily composed of ice crystals with various shapes having maximum dimensions ranging from about 20 μm to 2000 μm (e.g., Heymsfield and Platt 1984). The scattering properties of hexagonal ice crystals differ considerably from spherical particles (Liou 1986). Because of the complexities involved in computing scattering by hexagonal solids, cylindrical columns have been used to approximate hexagonal crystals in radiative transfer calculations (e.g., Liou 1973). More recently, however, Takano and Liou (1989a) have solved the radiative transfer equations for randomly oriented hexagonal plates and columns. Their results are the most realistic to date in that they reproduce certain well-known cirrus optical phenomena.

Absorption plays the dominant role in IR extinction in cirrus clouds. Some theoretical investigations (Liou and Wittman 1979; Stephens 1980), however, have shown that scattering effects may also be significant at IR optical depths greater than ~0.1. An IR radiance measured by a satellite over cirrus clouds, therefore, is the product of both absorption and scattering processes in the cloud, as well as the transmission of radiation from below the cloud (Platt and Stephens 1980). It is generally assumed, however, that scattering effects are negligible so that the observed emittance is considered to be the absorption beam emittance.

Empirical studies have also shed some light on the VIS reflectance–IR emittance relationship. Platt (1973) developed techniques for deriving cloud visible and infrared properties from a ground-based lidar and an upward-looking infrared radiometer. The backscattere intensities measured with the lidar are used to defin cloud base and top heights. Cloud emittance was de rived from the observed downwelling IR radiance. Plat and Dilley (1979) presented emittance results from set of observations taken over Australia. Platt et a (1980) used lidar and satellite VIS–IR data to estimat the dependence of beam emittance on VIS cloud re flectance for a limited set of viewing and illuminatio conditions over Colorado. Their results are more con sistent with theoretical scattering from ice cylinder than with scattering from ice spheres. Aircraft radic metric measurements taken over New Mexico (Pal tridge and Platt 1981) have also been used to determin the radiative characteristics of cirrus clouds as relate to the cloud ice water path. Those results provide fur ther evidence that real clouds scatter more like cylinder than spheres. Platt (1983) combined the results fron previous studies and used them to explain the char acteristics of two-dimensional bispectral histograms c VIS–IR data observed from a geostationary satellite Theoretical calculations of reflectance and emittanc for typical cirrus clouds were consistent with the sat ellite data taken over areas of suspected cirrus clouds While that study provided encouragement for using bispectral approach to retrieving cirrus properties fron bispectral data, it also highlighted some of the diffi culties that are likely to be encountered with such technique. Platt and Dilley (1984) used lidar and sola radiation measurements to measure part of the single scattering phase function of real cirrus clouds. Thei results fell within the range of laboratory measurement and theoretical calculations for hexagonal crystals. A analysis of a large sample of ground-based lidar an infrared data taken over Australia (Platt et al. 1987 showed that the average emissivity of cirrus clouds i primarily a function of the midcloud temperature Though fraught with significant uncertainties, tha study also indicated that the theoretical value of th ratio of visible extinction to infrared absorption fo cirrus clouds may be too low.

From these previous studies, it appears that:

1) cirrus cloud scattering properties are similar t those of hexagonal crystals resulting in reflectance pat terns that are unlike those from spheres;

2) scattering of IR radiation may be important i determinations of IR optical depths; and

3) the ratio of VIS extinction to IR absorption coef ficients is between ~1.8 and 4.0.

The full impact of these results on using a VIS–IR bi spectral method for retrieving cirrus properties is un known. Differences between ice crystal and wate droplet bidirectional reflectance patterns will introduc errors into the retrieved VIS optical depth. Use of a observed beam emittance with a theoretical model tha assumes absorption only may affect the emittance es timation. Finally, uncertainties in the extinction rati

(scattering efficiency) may cause significant errors in the estimation of IR optical depth.

In this paper, the relationship between VIS reflectance and IR emittance is examined using data taken during the First ISCCP Regional Experiment (FIRE) Cirrus Intensive Field Observations (IFO; see Starr 1987). Ground-based and aircraft lidars are used to define the vertical locations of the cirrus clouds, while satellites provide measurements of VIS and IR radiances. Both VIS and IR optical depths are computed from the reflectance and emittance data covering a range of solar zenith angles missed in previous studies. These relationships are derived to provide a means for the application of a bispectral cirrus parameter retrieval algorithm over the FIRE IFO region. Results are presented for the entire IFO period with emphasis on 27–28 October 1986, the case study period. The data presented here also constitute an initial source for developing cirrus bidirectional reflectance models and may be used to help validate the models employed in the ISCCP algorithm.

2. Data

a. Lidar measurements

Lidar backscatter data were taken from four different sources—three surface and one airborne. The lidars and their operating systems and data products have been described elsewhere. Thus, only a brief description of sources and their uses in this study are given here.

The University of Utah mobile polarization lidar (see Sassen et al. 1990) was located at Wausau, Wisconsin (WAU; 45.0°N, 89.7°W). The NASA Langley ground lidar (Sassen et al. 1990) was situated at Ft. McCoy, Wisconsin (FMC; 43.9°N, 90.8°W), while the University of Wisconsin High-Spectral Resolution Lidar (Grund and Eloranta 1990) was in Madison, Wisconsin (MAD; 43.1°N, 89.4°W). These ground systems acquired nearly continuous lidar backscatter profiles during the cirrus days of the IFO with especially good coverage during the case study period. The lidar returns are used to define the cloud base and physical thickness. Under conditions of small attenuation and constant backscatter-phase function, the backscatter intensity profiles indicate the vertical distribution of cloud extinction. A time series of these lidar returns shown in Fig. 1 define the outlines of the cirrus clouds as they passed over FMC during the afternoon of 28 October. Solid black areas define the most intense cloud backscatter. Grey denotes less backscatter and white indicates no cloud. Vertical stripes represent missing data. Cloud-top altitude is fairly constant at ~11 km. Cloud base changes from ~8 km to 10 km approximately every half hour. In the morning, cloud base was observed at ~7 km, while cloud top varied between 8 km and 11 km. A similar variation is also seen in the WAU estimated volume backscatter coefficients shown in Fig. 2 for the morning of 28 October. Darker portions

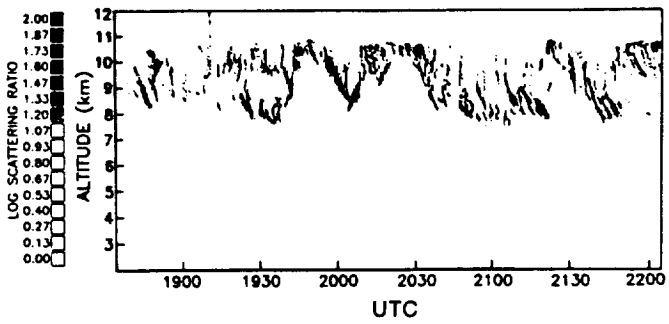

FIG. 1. Lidar backscatter ratios from cirrus clouds passing over Ft. McCoy during 28 October 1986.

of the plot correspond to higher backscatter coefficient values. The particle backscattering efficiency depends on cloud particle shape and phase. Further details of the lidar returns are reported in the cited references.

Three parameters are derived from plots like those in Figs. 1 and 2 by averaging the data within ±15 min of the UTC (Coordinated Universal Time) half hour plus 5 min. All times, however, will be given here to the nearest half hour. Cloud-top altitude, z_t, and cloud-base altitude, z_b, are defined as the average altitudes of the highest and lowest nonclear-air backscatter returns, respectively. Similarly, the cloud thickness is $h = z_t - z_b$. Mean cloud height (approximately cloud center height), z_c, is the backscatter-intensity weighted average height of the cloud. It corresponds roughly to the altitude below which 50% of the lidar backscatter is accumulated. These parameters were estimated graphically for the FMC and WAU sites, while a computer analysis was applied to the MAD results. The value of z_c for MAD corresponds to the midpoint in optical thickness independent of cloud attenuation (see Grund and Eloranta 1990). Since the clouds are advecting over the fixed surface sites, the averaged lidar data correspond to a thin vertical cross section taken out of some cloud volume. It is assumed that the cross-section-averaged data represent the mean conditions of that volume.

These same parameters were also derived from the down-looking lidar backscatter plots reported by Spinhirne et al. (1988) for selected flight tracks of the high-flying, NASA ER-2 aircraft over the IFO area. Shorter time averages were used since the plane's motion greatly increased the cirrus advection rates relative to the lidar. In some instances, the clouds were too thick for complete penetration by the ground-based lidars. To determine these occurrences, the cloud altitudes estimated from the ground were compared to those determined from the nearest aircraft flight. On most days, there was good agreement between the surface and airborne lidars. The thick clouds observed on 22 October required use of the aircraft lidar to estimate z_t. At other times when no aircraft data were available for comparison, a different approach was used to estimate z_t (see section 3a).

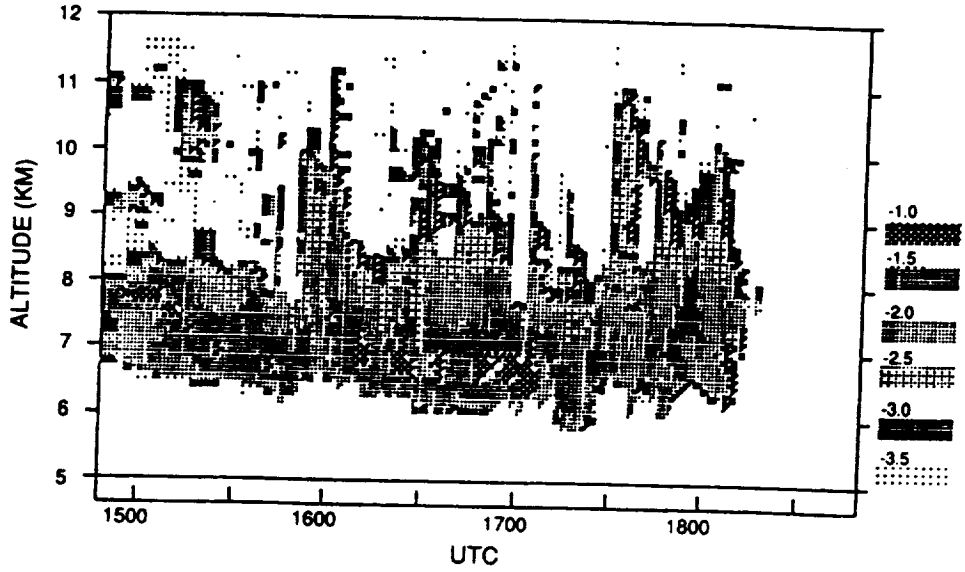

FIG. 2. Estimated lidar volume extinction efficiencies from cirrus clouds over WAU 28 October 1986.

b. Satellite radiances

Half-hourly VIS and IR data from the Geostationary Operational Environmental Satellite (GOES) were resolved to 4-km pixels by averaging and replication of 1-km VIS and 4-km × 8-km IR pixels, respectively, for most times. When the full-resolution data were not available, 8-km pixels derived by pixel averaging (VIS) and sampling (IR) were used. The pixels were navigated to ±8 km as in Minnis and Harrison (1984a). Pixel pairs were extracted for areas within 0.35° longitude and 0.25° latitude of the surface lidar sites. These areas correspond to cloud advection at wind speeds of ~30 m s^{-1} for a half-hour interval. Strips of pixels, 4(2) pixels wide, along the wind vector at z_c centered over the surface site were then taken from the 4 km(8 km) resolution areas. The satellite data corresponding to the ER-2 flight track were extracted for a strip centered on the flight track. This strip is approximately 30 km wide and 100 km long.

Two-dimensional histograms of the VIS and IR radiance pixel pairs were formed from the strips of extracted data. The VIS data, stored as counts, D (where $0 < D \leq 63$), in the histogram were converted to radiance and VIS reflectance, ρ, using the calibration of C. H. Whitlock (1989, personal communication) where

$$\rho = (0.1624D^2 - 8.3)(526.9\mu_0)^{-1},$$

and μ_0 is the cosine of the solar zenith angle θ_0. The raw IR data are given as equivalent blackbody temperatures, T, and are converted to radiance with the Planck function, $B(T)$, evaluated at 11.5 μm. Note that all radiometric quantities discussed in this study are spectral quantities, either VIS or IR, so no subscripts denoting spectral dependence are given.

A similar set of histograms was derived from the NOAA-9 Advanced Very High Resolution Radiome (AVHRR) Global Area Coverage (GAC) 4-km d for the 0.35° × 0.25° areas over the surface sites. T NOAA-9 daytime pass over the areas occurred betwe 2000 and 2130 UTC (~1430 local time). Radian from channels 4 and 5 were averaged to produce IR radiance corresponding to the GOES 11.5-μ channel. The AVHRR VIS data were taken fr channel 1 and converted to reflectance using the ca brations of C. H. Whitlock (1989, personal comm nication) where

$$\rho = (0.6060D_A - 22.0)(519.4\mu_0)^{-1}$$

and D_A is AVHRR 10-bit count.

Solar zenith, satellite zenith θ, and relative azimu ψ angles were computed for each set of measuremen from GOES-6 located over the equator at approx mately 97°W. This location yielded a value of $\theta \sim 5$ for the ground sites. Relative azimuth angles were co fined to the backscattering hemisphere for GOES. T orbital precession of the NOAA-9 produces a variatio in θ between 0° and 70° over a given site every 4- days. Because of its cross-track scan pattern, t AVHRR views a given site from relative azimuth angl that lie in both the forward and backward hemisphe at a nearly constant skew to the solar plane. The ske depends on both the solar and site latitudes. Conse quently, a range of solar zenith angles with constan viewing angles is covered using the GOES, while a rang of viewing angles at a relatively constant θ_0 is covere with the AVHRR.

Days when cirrus were observed over the IFO wi out substantial low-cloud interference are referred t as cirrus days. The times used in this study when lida and satellite data coincided with cirrus are listed i Table 1.

TABLE 1. Times and locations of lidar-satellite data used in this study.

Site	Day	Month	Times (UTC)
FMC	22	October	1300, 1330, 1400, 1600, 1630, 1700, 2000
	27		2030, 2100
	28		1330, 1400, 1430, 1500, 1600, 1700, 1900
			1930, 2000, 2030, 2100, 2130, 2200
	30		2000, 2030
	1	November	1800, 1900
	2		1900, 2000, 2100
MAD	28	October	1330, 1500, 1600, 1700, 1800, 1930, 2000
			2030, 2100, 2130, 2200
WAU	22	October	1300, 1330, 1400, 1430, 1600, 1630, 1700, 1800
			1830, 1900, 1930, 2130, 2200
	28		1500, 1600, 1700, 1800, 1900, 1930, 2000, 2030
			2100, 2130
	30		2130, 2200
	1	November	1800, 1900, 2000
	2		1700, 1800, 1900, 2000, 2100

c. *Temperature data*

Soundings from Green Bay, Wisconsin, determined the temperature–height relationships for all of the data. Linear interpolation was used to estimate half-hourly soundings from the six-hourly data. Cloud-top temperature, T_t, corresponds to z_t on the soundings. Mean cloud temperature, T_c, is found from z_c. Surface temperatures taken every six hours at MAD, WAU, and Lone Rock, Wisconsin (Hahn et al. 1988), and occasionally at the FMC site, were used to supplement the clear-sky temperatures derived from the satellite data as described below.

The clear-sky temperature, T_s, is the equivalent blackbody temperature for clear scenes. It is estimated in several different ways. The first order estimate is taken from the initial results of Minnis et al. (1990), which applies the techniques of Minnis et al. (1987) to 0.5° regions within the greater IFO area. That approach sets a VIS threshold ~2 counts above the clear-sky count, D_s (see section 3). All pixels considered to be clear must be darker than this threshold and have a temperature that is no more than 3 K colder than the maximum observed temperature. The 4 K range for clear pixels, roughly double the typical value over Wisconsin land areas, allows for shading effects in partly cloudy scenes. The average temperature of the clear pixels is the initial value of T_s. Surface air temperatures, T_g, are also taken from nearby ground stations. A rough correction is applied to these temperatures to adjust for atmospheric attenuation and the difference between the temperature of the surface skin and the air at shelter height. The resulting estimate of clear-sky temperature is T_s. An example of the relationship between T_s and T_g is shown in Fig. 3 for a region including FMC during 27 October 1986. Note that the difference between T_s and T_g constitutes the correction to determine T_s from T_g. It varies with local time (6 hours less than UTC) from positive values in the morning to negative values in the afternoon, behavior typical of land surfaces (e.g., Minnis and Harrison 1984a).

The initial value of T_s for the ground site is compared to the values for the surrounding regions to check for cirrus contamination of the clear-sky temperature. If T_s for the ground site is not within 2 K of the warmest value found for nearby regions, then its value is reset to that of the warmest value. The 2 K limit is typical of the range in T_s over relatively flat homogeneous areas. If extensive overcast prevents the calculation of T_s, $T_s = T_g$.

The AVHRR clear-sky temperatures are first estimated using T_s derived from the AVHRR data. If that result is lower than the corresponding GOES estimate of T_s by 2 K, then the AVHRR value of T_s is reset to the GOES value. It is assumed that the warmer of the two values is less cloud contaminated. Because of limb-darkening effects, the AVHRR value of T_s may be up to 2 K colder than the GOES value and still be valid. In warmer, moister atmospheres, greater limb-darkening effects are expected.

3. IR and VIS parameter analyses and results

a. *Emittance calculations*

Neglecting IR scattering effects, the observed cloud beam emittance is given here as

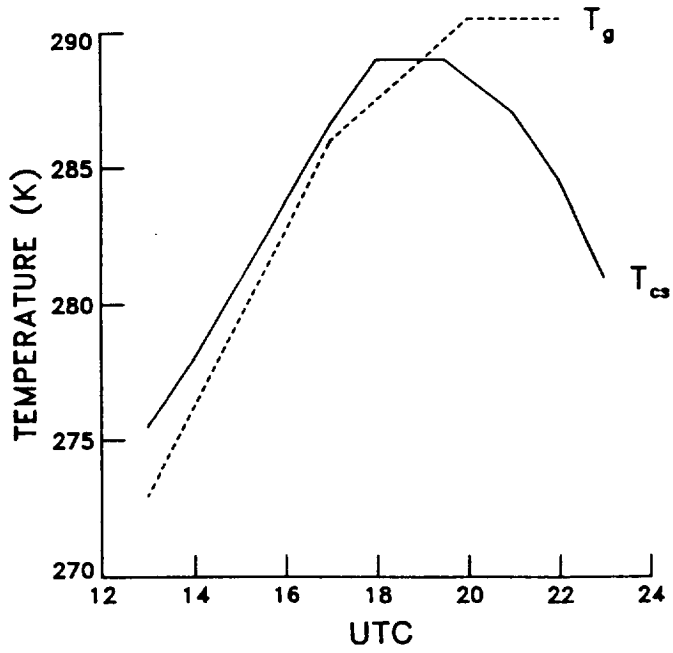

FIG. 3. Comparison of clear-sky and shelter air temperatures over FMC 27 October 1986.

$$\epsilon_b(\theta) = [B(T) - B(T_s)][B(T_z) - B(T_s)]^{-1}, \quad (1)$$

where T_z is the temperature at some altitude z corresponding to the cloud. The mean clear-sky equivalent blackbody temperature over the area of interest, T_s, has a weak dependence on θ.

Cloud beam emittance is calculated twice for each set of lidar-radiance data using $T_z = T_c$ and $T_z = T_t$. The former value, which corresponds to the quantity used in most previous studies (e.g., Platt et al. 1980), may be more representative of the actual radiating part of the cloud. It does not necessarily correspond to the center of the cloud. The actual cloud-top temperature defines the vertical limit of the cloud. Emittances are computed using both temperatures to determine if there is a relationship between them that may be used to better define the physical boundaries of the cloud from the satellite data.

Due to angular effects, the values of T_c may require some adjustment from the initial lidar values. It is unlikely that a value of $\epsilon_b = 1$ will be measured at a useful satellite zenith angle using T_t because of the low density of particles in the upper portions of the cloud. On the other hand, $\epsilon_b(T_c)$ may be greater than one for some thick cirrus clouds. Although emittances greater than unity may be possible due to scattering enhancements of the upward radiance (Platt and Stephens 1980), the uncertainties in z_c for thick clouds preclude any definitive measurements of $\epsilon_b > 1$. Thus, if $\epsilon_b > 1$, T_c is decreased until the average value of ϵ_b for a given reflectance is less than or equal to one. While this limit is reasonable, it is somewhat arbitrary resulting in increased uncertainty in the true value of T_c for thick clouds.

During initial processing of the data, it was determined that the maximum emittance found using T_t was ~0.86, except for those cases with cloud cover too dense for complete penetration of the lidar beam. To identify and correct the exceptions, a new estimate of T_t was computed whenever T_c was adjusted as explained above. This new estimate, T_t', is determined from the following formula, which forces the cloud to have the maximum observed emittance:

$$B(T_t') = [B(T) - 0.14B(T_s)]/0.86.$$

The resulting value was then compared to T_t. If $T_t' < T_t - 3$ K, then T_t is reset to T_t'. The 3 K allowance (~0.5 km) is made to account for uncertainties in the lidar-determined cloud-top, due to time averaging and unknown penetration depth in thicker cloud. The result was then compared to the tropopause temperature using the assumptions that the cloud occurs in the troposphere and the tropopause temperature is the coldest in the troposphere. If T_t is colder, it is reset to equal the tropopause temperature. The value of z_t was then adjusted to correspond to the final value of T_t.

It is also assumed that

$$\epsilon_b = 1 - \exp(-\tau_e/\mu), \quad (2)$$

where τ_e is the IR absorption optical depth ar $= \cos\theta$. Based on the results of Platt and Stepl (1980), it is expected that the viewing zenith a dependence of ϵ_b will not depart significantly from Values of beam emittance derived with AVHRR may be adjusted to the GOES viewing zenith a with this relationship.

The vertical emittance from (2) is

$$\epsilon_a = 1 - \exp(-\tau_e).$$

It is assumed here that scattering effects are negli in the upwelling direction. Thus, τ_e is equivaler the IR absorption optical depth and ϵ_a is equal tc vertical emittance.

b. *VIS reflectance and optical depth calculations*

Values of clear-sky reflectance ρ_s and clear-sky c D_s were computed for each region using the 0.01° c sky albedo, α_s, map of the IFO area (42°N–4 87°W–92°W) constructed by Minnis et al. (1990) f GOES data at each half hour. Clear-sky reflectance any latitude λ and longitude ϕ of the grid at time estimated as

$$\rho_s(\lambda, \phi, t, \theta_0, \theta, \psi) = \alpha_s(\lambda, \phi, t, \theta_0)\chi_s(\theta_0, \theta, \psi),$$

where χ_s is the anisotropic reflectance factor with va given by the model of Minnis and Harrison (198 D_s was determined by ρ_s using the VIS calibrati The value of θ_0 varies by a few degrees over the time period, while the values of α_s were normalize a single value of solar zenith angle designated θ_{0_t} account for these variations, $\alpha_s(t, \theta_0) =$ $\theta_0)\mu_0/\mu_{0_t}$, where $\mu_{0_t} = \cos\theta_{0_t}$. The clear-sky diffus bedo is

$$\alpha_{sd} = \int \alpha_s(\theta_0)\mu_0 d\mu_0 \Big/ \int \mu_0 d\mu_0,$$

integrated over $\mu_0 = 0, 1$. The value of α_{sd} is set e to $\alpha_s(57°)$ in this study since the full range of s zenith angles is not observed at the time and lati of the IFO, the true value of α_{sd} is usually equiva to α_s measured at $\theta_0 \approx 53°$, and 57° is the lo observed θ_0 for this dataset.

Cloud reflectance, ρ_c, is estimated with a varia the simple physical model used by Platt et al. (19 That is,

$$\rho = T_a\rho_c + \rho_s T_c T_u + \alpha_{sd}(1 - \alpha_d)(1 - T_c - \alpha_c),$$

where ρ is the measured reflectance, α_c is the c albedo at θ_0, χ_c is the anisotropic reflectance facto the cloud, and $\rho_c = \alpha_c\chi_c(\theta_0, \theta, \psi)$.

This model assumes that all ozone absorption oc above the cloud (first term) and all Rayleigh and a sol scattering is confined to the layers below the cl The second term in (5) accounts for direct sola diation, which passes through the cloud, reflects f the surface, and passes back through the cloud ir

direction of the satellite. The third term accounts for the radiation that passes down through the cloud via multiple scattering, reflects diffusely from the surface below the cloud, and returns through the cloud scattered in the direction of the satellite.

Using the parameterization of Rossow et al. (1988), the transmittance of the air above the cloud is

$$\Upsilon_a = \exp[-u(0.085 - 0.00052u)(1/\mu_0 + 1/\mu)],$$

where u is the ozone abundance in cm-STP. The value used here, $u = 0.32$ cm-STP, is the average of the mid-latitude winter and summer standard atmospheres above 10 km from McClatchey et al. (1973). Platt et al. (1980) implicitly assumed that $\Upsilon_a = 1$. The current model accounts for ozone absorption in the Chappius bands.

The transmittance of the cloud to direct solar radiation at θ_0 is

$$\Upsilon_c = \exp(-\tau_v/2\mu_0), \quad (6)$$

(see Platt et al. 1980). Similarly, the direct transmittance from the surface through the cloud along the satellite line of sight is

$$\Upsilon_u = \exp(-\tau_v/2\mu).$$

The visible optical depth is reduced by a factor of two for the direct transmittance because at least half of the radiation scattered out of the beam is actually diffracted in the forward direction (Takano and Liou 1989a). Clear-sky reflectance along the satellite line of sight is ρ_s and α_{sd} is the effective clear-sky albedo to diffuse radiation directly below the cloud. Due to the relative homogeneity of clear-sky reflectance over the IFO region, it is assumed that α_{sd} and ρ_s may be computed from the same data. The albedo of the cloud to diffuse radiation is α_d.

In addition to values for the clear-sky terms, the solution of (5) for ρ_c requires specification of τ_v and χ_c. VIS optical depth is estimated by iteration on (5) using a linear interpolation of the relationships between μ_0 and α_c for randomly oriented hexagonal columns (length, 125 μm; width, 50 μm) in Fig. 4 of Takano and Liou (1989b). Similar interpolations are used to estimate $\alpha_d(\tau_v)$, where

$$\alpha_d(\tau_v) = \int_0^1 \alpha_d(\tau_v, \mu_0)d\mu_0 \Big/ \int_0^1 \mu_0 d\mu_0.$$

For a given measurement, (5) is solved iteratively using an initial guess of cloud albedo such that $\Upsilon_c = \Upsilon_u = 1 - \alpha_c$. A value for τ_v is determined from this initial guess using the theoretical data. A limit of 20 iterations is imposed to achieve an absolute difference of less than 0.001 between the guess and the computed value of α_c. Generally, fewer than five iterations are required. Since α_c must be greater than zero, α_c is set to 0.001 for initial guesses that are less than or equal to zero. If $\tau_v < 0$, $\alpha_d < 0.001$, or $\alpha_c \leq 0.001$ after any iteration, it is assumed that τ_v is indeterminate and the data are not used. The causes for these indeterminate cases (e.g., shadowing of the surface by adjacent clouds or inadequate specification of the cloud reflectance anisotropy) are discussed later.

A value for χ_c, which depends on τ_v and the cloud microphysics, is needed to determine α_c from ρ_c. No models of χ_c are currently available for ice clouds in terms of τ_v. Because of favorable angles Platt et al. (1980) were able to assume that $\chi_c = 1$. However, most empirical and theoretical bidirectional reflectance models for cloudy scenes (e.g., Suttles et al. 1988) reveal a systematic decrease in χ_c with θ_0 for the angles used in this study. The cloudy scene bidirectional reflectance model developed by Minnis and Harrison (1984b) is used initially to estimate χ_c. That model's reflectance anisotropy is similar to other empirical and theoretical models (Stuhlmann et al. 1985). The inclusion of all cloud types in its derivation should produce a reflectance pattern that combines the scattering properties of both ice and liquid water clouds. New values of χ_c, derived after the initial analysis, are used to reanalyze the data to provide better estimates of VIS optical depth.

The data were preprocessed to define limits to eliminate pixels containing low clouds and those scenes containing only thick clouds. Underlying low clouds confuse the interpretation of cirrus radiances. Thick clouds increase the uncertainty in the determination of T_c, T_t, and ϵ_b. A simple filter of the form,

$$\epsilon_b = 1 - \exp(-k\alpha_c/\mu), \quad (7)$$

where k is a regression coefficient, was used to eliminate low clouds. This formula gives a first approximation to the relationship between ϵ_b and cloud albedo. The rationale for its use and the details of the filtering are described in appendix A. The data were also screened for partially cloud-filled pixels as detailed in appendix B.

c. *Results and discussion for midcloud temperature emittances*

All results discussed in this section are based on $T_z = T_c$ in (1). Examples of the two-dimensional GOES histograms used in this analysis are shown in Figs. 4a and 4b for 1500 UTC over FMC. The latter represents a cirrus case (see Fig. 1) on 28 October, while the former, taken during the previous day, is typical of clear conditions. Maximum clear-sky reflectance for this hour is denoted with the dashed line in Fig. 4a. Some of the cold, apparently cloudy pixels in Fig. 4b are no brighter than the clear pixels in Fig. 4a. Moreover, some of these pixels are actually darker than the cloud-free pixels. Depending on χ_c and τ_v, some of the cold, dim pixels yield a positive value of α_c in the solution of (5). Those pixels with indeterminate α_c and $T < T_s - 3$ K are hereafter referred to as "dark" pixels.

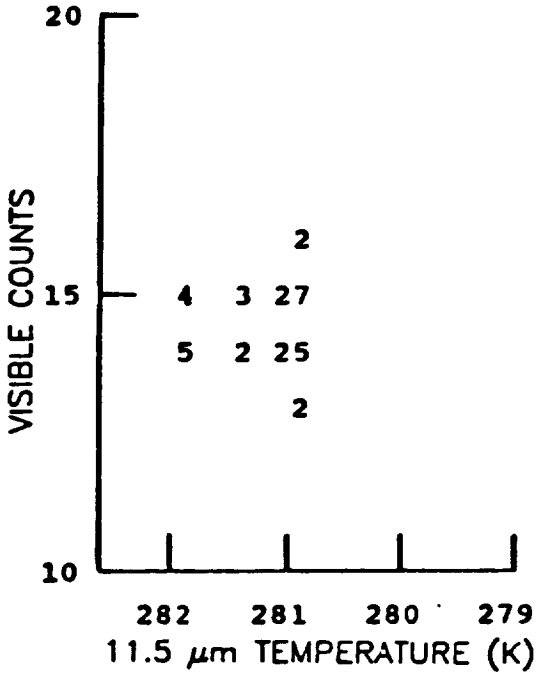

FIG. 4a. VIS–IR histogram of GOES pixels over FMC at 1500 UTC 27 October 1986 (numbers denote frequency of occurrence of temperature-count pairs).

They are not used to solve (7). Their impact and origins are discussed in section 4d. The cloud emittances are plotted in Fig. 5a against the measured reflectances for the case in Fig. 4b. Eliminating the dark pixels and applying (5) to the data in Fig. 5a yields the cloud albedo values. Averaging the emittances for a given albedo produces the mean values and the standard deviations plotted in Fig. 5b. The solid line represents the solution to (7) using the average value of $k = 5.1$. The mean beam emittance and VIS optical depths for the data used in Fig. 5b are $\bar{\epsilon}_b = 0.38$ and $\bar{\tau}_v = 0.59$.

The data from FMC in Fig. 5b for this hour are compared to those from MAD and WAU shown in Fig. 6. Apparently, the clouds over WAU are much denser than those over MAD, while the MAD observations are similar to those over FMC. Values of T_c differed by only 1 K among the sites, while T_t ranged from 225 K at WAU to 217 K at MAD. Depolarization ratios derived from the lidar returns indicated intermittent liquid layers during the morning of 28 October, especially at ~1500 UTC. Those liquid layers may be the source of the larger emittances over WAU. Data from all three sites were combined, averaged, and fit with (7) yielding $k = 5.6$. The scatter in the means between the sites at a given hour is of the same order as that for different hours at the same site as seen in Fig. 7 for FMC at 3 times during 28 October.

1) GOES-SURFACE LIDAR RESULTS

A summary of the results for the case study 27–28 October is given in Table 2. Cloud-top heights range from 9.5 to 11.0 km at all three sites. The cloud-center temperatures vary by about 25 K. Cloud optical depths were much greater over WAU than over the other sites. Dark pixels were found more often over FMC and MAD than over WAU.

Due to dropouts, the only data available for 1500 UTC during the primary IFO cirrus days occurred on 28 October. Data from other days were available for most of the afternoon hours. The combined datasets permitted coverage of the full range of emittances at a given hour as illustrated in Fig. 8 for 2000 UTC. Data for all of the hours used in the case study and the entire IFO analyses are shown in Figs. 9a and 9b, respectively. The clouds over the area during 27–28 October were generally thinner with lower emittances than most of those observed during the other days. The combined datasets (Fig. 9b) yield a large number of samples for $\epsilon_b < 0.5$ and $\epsilon_b > 0.8$ and relatively few for intermediate values of ϵ_b. Apparently, the cirrus, which occurred during the IFO, tended to be either very thick or rel-

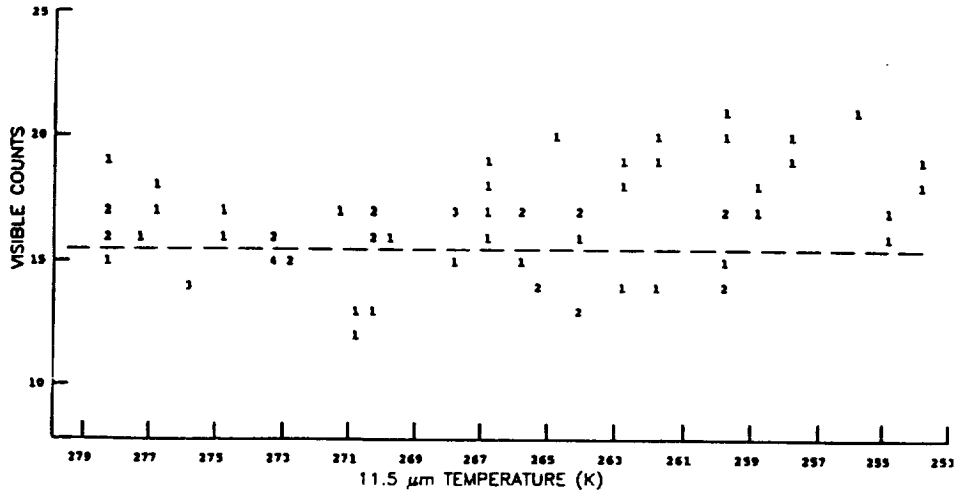

FIG. 4b. VIS–IR histogram of GOES pixels over FMC at 1500 UTC 28 October 1986. Dashed line refers to maximum clear-sky count.

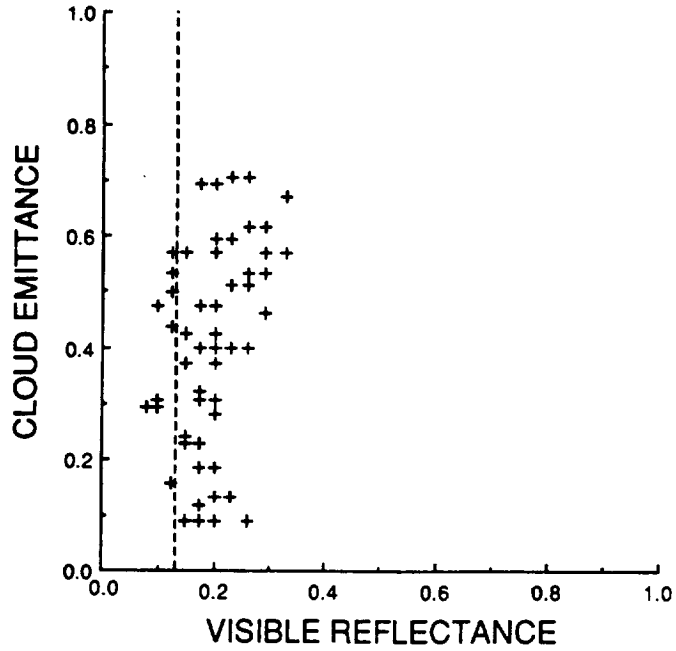

FIG. 5a. Cloud emittances and observed reflectances for $T < T_s - 3$ K derived from Fig. 4b. Dashed line refers to maximum clear-sky reflectance.

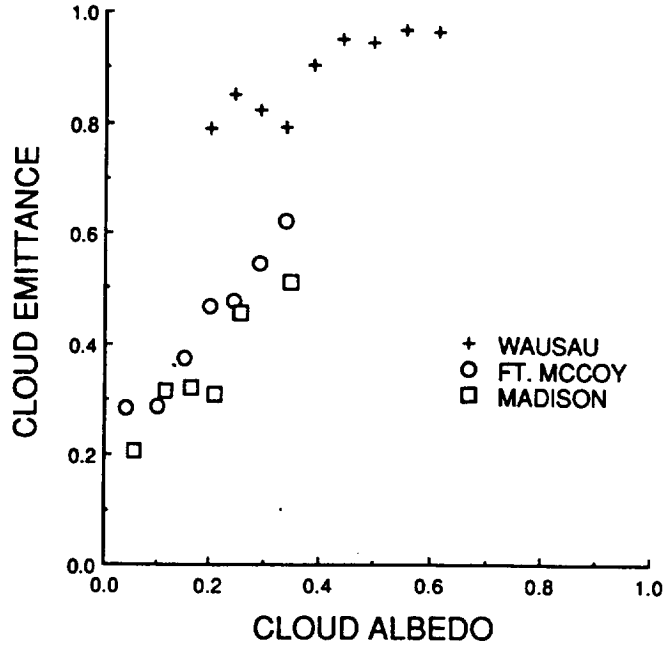

FIG. 6. Average cloud emittance versus cloud albedo at 1500 UTC 28 October 1986 over three sites from GOES VIS-IR data.

atively thin. Perhaps, a longer time period would produce more uniform sampling. No data are found for $\epsilon_b < 0.08$ since no clouds are recognized if $T > T_s - 3$ K.

Table 3 summarizes the values of τ_v derived from all of the GOES-surface IFO data (Fig. 9b) and from case study data only (Fig. 9a) for each relevant time. The average scattering angles, Θ, between the sun, satellite, and scene are also listed in Table 3. Visible optical depths observed during the case study are less than half of those observed for all of the IFO cirrus days.

The mean vertical emittance is given as a function of temperature in Fig. 10. The dashed line corresponding to the results from Fig. 7a of Platt et al. (1987) is included for comparison. Although there is a general increase in ϵ_a with increasing cloud temperature, the

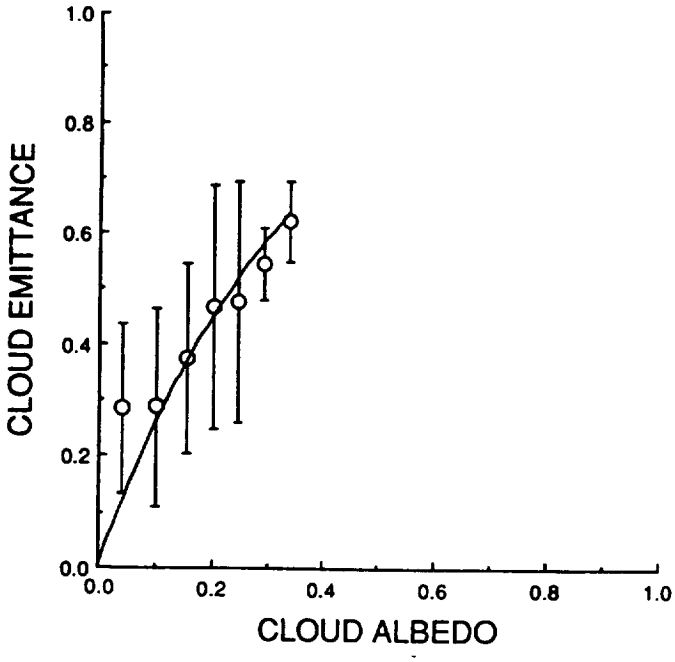

FIG. 5b. Cloud albedos and mean cloud emittances derived from Fig. 5a without "dark" pixels. Vertical lines represent standard deviations. The curved line denotes the regression fit to Eq. (7).

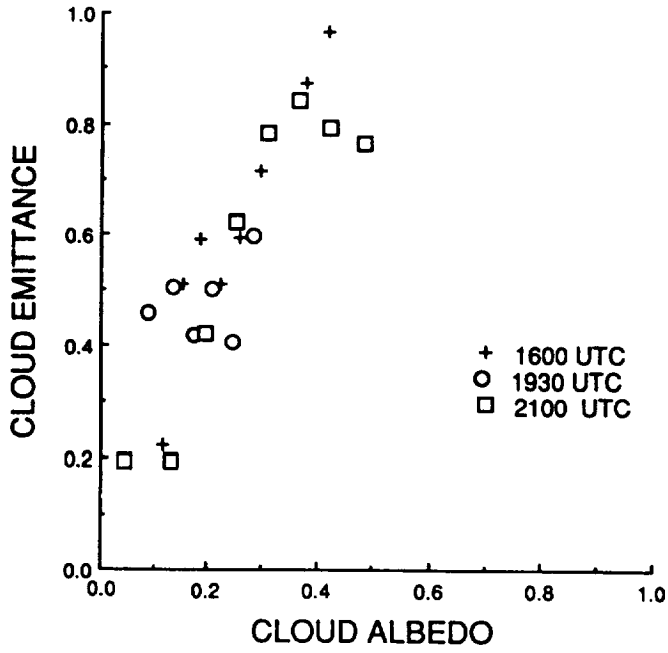

FIG. 7. Average cloud emittance and albedo at three times during 28 October 1986 over FMC from GOES VIS-IR data.

TABLE 2. Observed and computed cloud properties for October 1986 case study.

Site (Day)	Time (UTC)	T_s (K)	z_t (km)	h (km)	T_c (K)	T_t (K)	τ_e	τ_v	Dark pixel (%)	τ'_v	ξ
FMC (27)	2030	287.7	9.6	1.1	227.8	225.1	0.11	0.23	4	0.20	1.8
	2100	286.9	10.3	1.6	228.7	220.3	0.19	0.52	0	0.55	2.6
(28)	1330	278.3	9.5	2.1	237.9	227.7	0.22	0.12	0	0.22	1.0
	1400	279.7	11.0	1.3	231.6	216.8	0.14	0.16	5	0.21	1.5
	1430	280.5	11.2	1.5	230.0	215.6	0.18	0.32	11	0.38	2.0
	1500	281.6	10.1	1.3	239.4	222.5	0.31	0.62	7	0.65	1.9
	1600	283.0	10.0	3.0	240.1	223.2	0.80	1.77	0	1.61	2.1
	1700	287.9	10.4	1.9	223.0	219.6	0.23	0.95	0	0.74	3.6
	1900	285.4	10.8	2.1	227.5	217.1	0.23	0.64	0	0.45	1.9
	1930	285.5	10.9	2.6	228.9	216.6	0.41	0.99	3	0.79	1.9
	2000	285.9	11.0	1.9	224.4	216.3	0.41	1.05	0	0.87	1.9
	2030	284.8	10.9	1.7	220.7	216.4	0.62	1.78	6	1.55	1.9
	2100	280.9	10.7	2.4	230.7	216.7	0.79	1.41	5	1.53	2.0
	2130	281.2	10.8	2.2	226.3	216.4	0.44	0.75	11	1.33	2.7
	2200	276.8	10.9	2.4	221.7	216.1	0.32	0.30	0	0.87	2.4
MAD (28)	1330	278.4	10.8	3.4	237.9	217.9	0.16	0.18	3	0.35	2.2
	1500	280.2	10.8	4.2	242.8	217.7	0.24	0.65	2	0.68	2.0
	1600	281.7	10.6	3.7	241.9	218.5	0.58	1.18	0	1.07	1.9
	1700	284.8	10.5	4.3	240.4	218.8	0.40	0.98	0	0.75	1.9
	1800	289.1	9.8	3.2	229.4	224.6	0.14	0.95	0	0.75	5.2
	1930	287.7	10.7	1.8	222.1	217.3	0.10	0.26	3	0.13	1.2
	2000	286.5	10.7	1.8	221.7	217.1	0.10	0.55	7	0.43	4.4
	2030	286.6	10.7	3.1	223.3	217.1	0.34	0.86	3	0.76	2.2
	2100	286.0	10.5	2.4	223.3	217.2	0.29	0.56	33	0.59	1.9
	2130	284.5	10.8	4.0	232.2	216.4	0.55	0.46	3	0.73	1.2
	2200	281.1	10.5	4.2	237.4	216.8	0.44	0.27	13	1.24	2.
WAU (28)	1500	279.0	9.8	3.2	238.0	225.0	1.67	3.20	0	3.50	2.0
	1600	282.5	10.1	3.1	238.0	222.4	1.40	2.42	0	2.19	1.2
	1700	287.1	10.1	3.9	235.0	222.3	1.21	2.52	0	1.91	1.7
	1800	288.4	10.3	4.1	231.0	220.3	1.13	3.13	0	2.35	4.0
	1900	285.7	11.0	0.8	217.1	216.4	0.19	0.77	0	0.55	3.
	1930	283.9	10.9	2.1	226.4	216.6	0.30	1.03	0	0.82	2.4
	2000	284.4	10.9	2.9	236.1	216.5	1.04	2.42	0	1.93	1.3
	2030	285.4	10.7	3.1	231.0	216.9	1.34	3.73	0	3.11	2.0
	2100	284.1	10.6	3.2	234.0	217.0	0.36	1.43	7	1.66	3.2
	2130	279.7	11.0	1.0	217.0	216.0	0.29	0.45	1	0.76	2.

values derived for the case study are generally lower than the IFO means. The case study averages parallel those found by Platt et al. (1987) using ground-based observations in Australia. The mean value of ϵ_a found here for the case study results is 0.33, the same as that from Platt et al. (1987).

Cloud thickness versus T_c is shown in Fig. 11. Maximum average thickness is found at $T_c \approx 232$ K for the IFO and at $T_c \approx 241$ K for the case study. The case study values of h increase nearly monotonically with T_c. The IFO results show a tendency towards thinner clouds for $T_c < 220$ K and for $T_c > 240$ K. The thickest clouds were observed during 22 October and 1 November. During the case study, the observed clouds were 2.6 km thick on average compared to a mean thickness of 4.2 km during the remaining cirrus days of the IFO.

Cloud IR volume absorption coefficient, $\sigma_a = \tau_e/h$, is plotted against T_c in Fig. 12. The results reveal a trend of increasing extinction with T_c in the IFO data (correlation coefficient of 0.71). The average value σ_e is 0.20 for the case study data.

The variation of vertical emittance with T_c for tl IFO data differs from that found for the case study ar Platt et al. (1987), probably because of substanti differences in cloud depths. This difference in thickne is evident in Fig. 11 where the case study data, a subs of the IFO data, are also consistent with the results Platt et al. (1987), probably because of substanti ume absorption coefficients in Fig. 12 are not as we behaved as emittance and cloud thickness when co sidered as a function of T_c. Except for the highest ar lowest temperatures (which are poorly sampled), for the case study data is close to that observed by Pla et al. (1987). Differences between the IFO and ca study data are also seen in the behavior of σ_a suggesti that thickness is not the only discrepancy between tl case study and other IFO clouds. Vertical distributio of nongaseous cloud water content and particle shape sizes, and phase may also affect these differences.

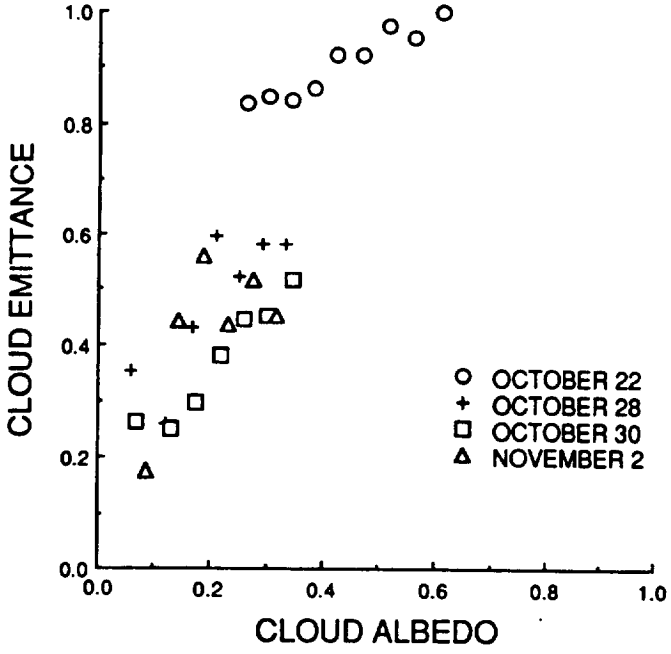

FIG. 8. Average cloud emittances and albedos from GOES at 2100 UTC over FMC during different IFO days.

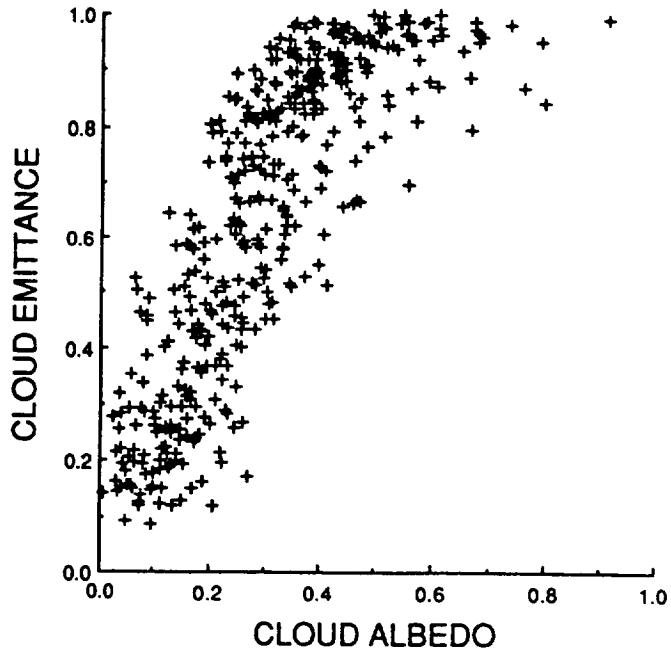

FIG. 9b. Same as Fig. 9a, except for all IFO scenes.

2) GOES/ER-2 CLOUD PARAMETERS

Table 4 lists the data and derived parameter values for the five cirrus matches between the GOES and ER-2 lidar for the case study days. Data taken during 27 October were located just outside the northwestern boundary of the IFO area. On 28 October the ER-2 was over Lake Michigan at ~1600 UTC, while it was near FMC at 1800 UTC. The three scenes at 1600 UTC correspond to small contiguous areas. The small optical depths indicate that the aircraft also sampled relatively thin clouds during the case study.

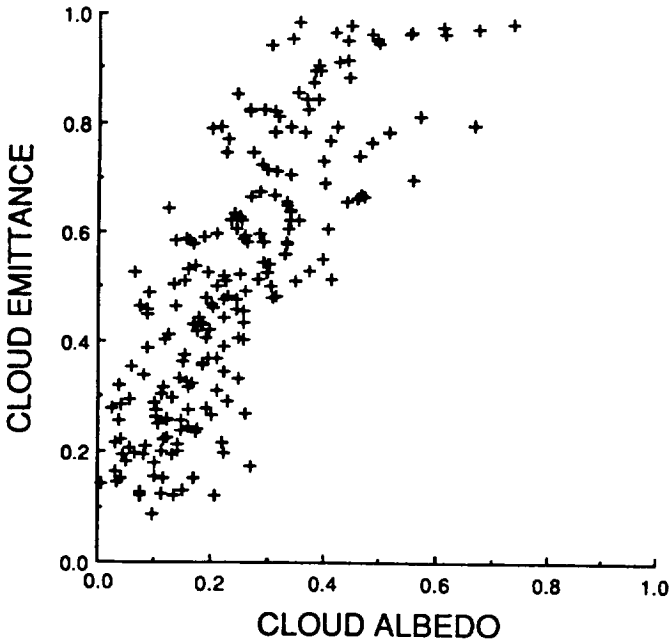

FIG. 9a. Average cloud emittance versus cloud albedo for all case study scenes from GOES over surface sites where $T_s = T_c$.

3) CLOUD PARAMETERS FROM AVHRR DATA

Figure 13 presents the averaged cloud emittance-albedo pairs derived from both AVHRR and GOES data taken for the 0.25° × 0.35° area over WAU on 28 October. Although the relative viewing angles were within ±8° for the two satellites, the absolute viewing conditions were different. The GOES viewed the region from the south, while the AVHRR viewed from the north with the solar plane almost midway between the two views. Discrepancies in the albedo range may be due to this misalignment (some dark pixels were found in the GOES results). Resolution differences, however, would tend to produce a smaller range in both albedo and emittance for the GOES (8 km) relative to the AVHRR (1 × 4 km^2) radiances as observed in Fig. 13. In general, the GOES data are very close to the AVHRR results except for the smaller values of α_c. The latter may be affected by the presence of "dark" pixels. The values for the AVHRR VIS and IR optical depths are ~10% greater than their GOES counterparts.

Another comparison of GOES and AVHRR results is given in Fig. 14 for data taken over WAU 2 November. The AVHRR viewed the scene with $\theta = 18°$ and $\psi = 38°$. The squares correspond to AVHRR data as reduced for the given viewing angles. AVHRR emittances corrected to the GOES viewing zenith angle using (2) are denoted with the crosses. The range in α_c is smaller for GOES than for the AVHRR, consistent with the resolution differences. In this case, the

TABLE 3. Reflectance parameters computed for all GOES-surface lidar data.

Time (UTC)	Cases (IFO)	θ (°)	ψ (°)	Θ (°)	Nominal (χ_c) All data (IFO) τ_v	ξ	Nominal (χ_c) Case study τ_v	ξ	Reanalyzed (χ'_c) All data (IFO) τ'_v	ξ'	Reanalyzed (χ'_c) Case study τ'_v	ξ'
1330	4	80.2	106.6	109	1.28	1.17	0.15	0.83	0.28	1.61	0.28	1.6
1400	3	75.6	112.6	117	2.21	1.42	0.17	1.12	3.22	2.32	0.21	1.5
1430	2	71.3	118.6	124	1.07	1.79	0.32	1.72	1.35	2.22	0.38	2.0
1500	3	67.9	125.7	131	1.72	2.02	1.72	2.02	1.87	2.15	1.87	2.1
1600	5	61.0	140.0	146	2.93	2.50	1.82	2.11	2.64	2.25	1.64	1.9
1630	2	57.8	147.7	153	2.59	1.85	—	—	3.06	2.18	—	—
1700	6	57.6	156.6	160	2.58	2.90	1.57	2.93	1.96	2.21	1.20	2.2
1800	6	57.3	174.1	173	2.43	2.96	1.95	6.21	1.92	2.33	1.48	4.8
1830	1	56.1	177.1	175	3.65	2.06	—	—	3.88	2.19	—	—
1900	7	59.9	169.0	168	1.62	3.12	0.69	3.43	1.82	2.12	0.49	2.3
1930	4	61.1	160.8	162	1.73	2.74	0.75	2.76	1.34	1.97	0.57	1.9
2000	8	65.0	153.6	154	2.07	2.68	1.69	2.87	2.27	2.26	1.35	2.3
2030	5	68.3	146.5	147	1.56	2.55	1.87	2.37	1.33	2.23	1.59	2.0
2100	6	72.8	140.3	140	1.07	2.07	1.02	2.19	1.17	2.24	1.12	2.3
2130	4	76.2	133.6	132	1.12	1.29	0.55	1.25	0.81	2.23	0.94	2.0
2200	5	81.2	128.1	125	0.80	0.84	0.28	0.70	1.04	2.30	0.80	2.3
Totals and means	71	67.2	145.4	—	1.69	2.13	1.04	2.17	1.80	2.19	1.11	2.1

AVHRR data produce a much lower minimum cloud albedo. The application of (2) appears to have produced very similar emittances for the two datasets, although there is a 20% difference in the average values of τ_e. The mean VIS optical depths differ by a factor of 2.

All of the coincident AVHRR and GOES data are summarized in Table 5. The AVHRR IR optical depths are consistently greater than the corresponding GOES values by ~0.1. This difference indicates the possibility of a calibration offset in the thermal channels. Despite this obvious bias, the good relative agreement in Fig. 14 between the corrected AVHRR emittances and the GOES emittances suggests that (3) is a reasonable approximation to the IR absorption optical depth. Any IR scattering effects that are ignored here are apparently

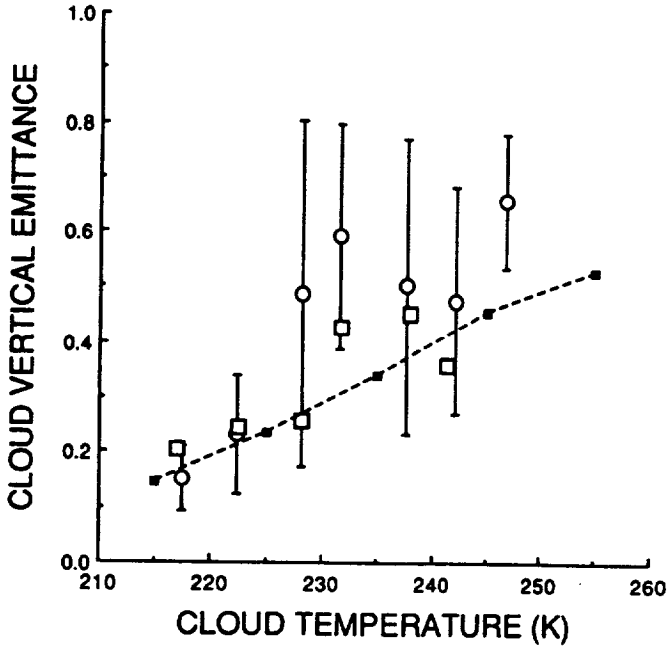

FIG. 10. Variation of cloud vertical emittance with cloud-center temperature for all IFO (circles) and case study (squares) data from GOES over surface lidar sites. Vertical lines denote standard deviations. Dashed line adapted from Platt et al. (1987).

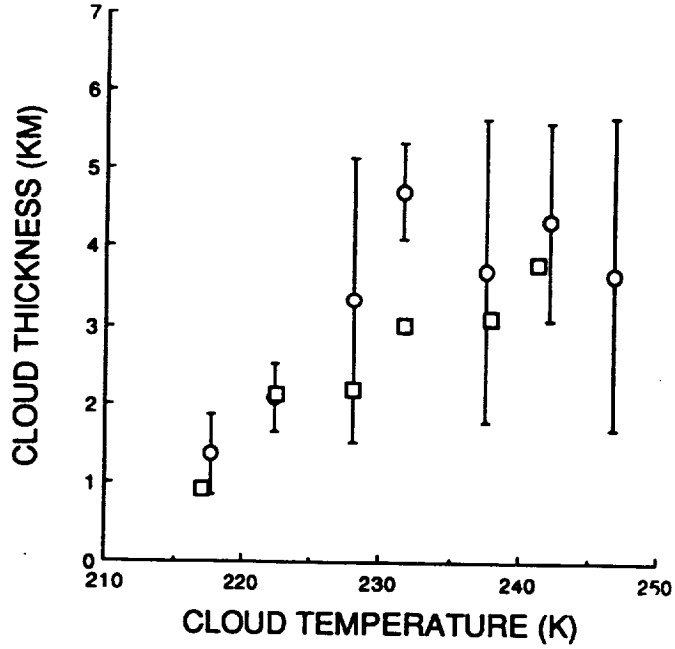

FIG. 11. Variation of cloud thickness with cloud-center temperature for all IFO (circles) and case study (squares) data from GOES over surface lidar sites. Vertical lines denote standard deviations.

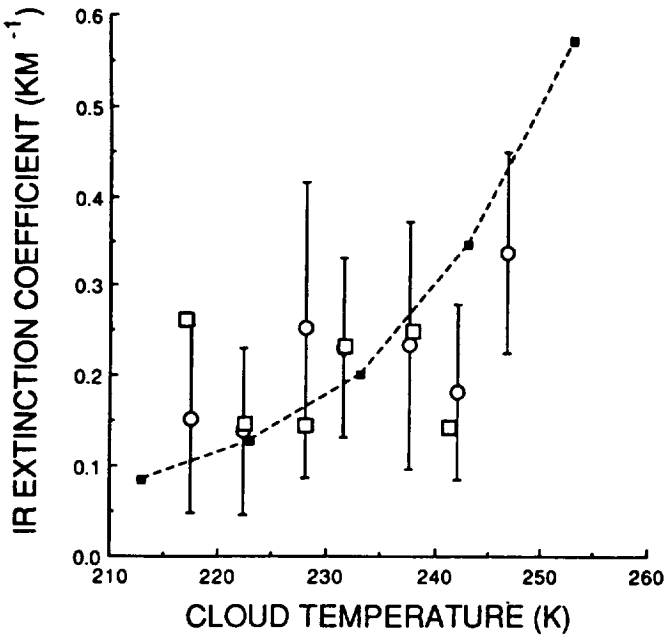

FIG. 12. Variation of infrared volume extinction (absorption) coefficient with cloud-center temperature for all IFO (circles) and case study (squares) data from GOES over surface lidar sites. Vertical lines denote standard deviations. Dashed curve adapted from Platt et al. (1987).

insignificant compared to the other error sources. Differences between the GOES and AVHRR values of τ_v vary from scene to scene. Even when the times and angles are very close and the data appear similar as in Fig. 13, there are substantial differences in τ_v. Over FMC during 28 October, there is good agreement between the parameters however. The outstanding differences may be attributable to a number of factors that are discussed in section 3e.

d. Results and discussion for cloud-top temperatures with GOES

The analyses discussed above were also performed for the GOES-derived emittances for $T_z = T_t$. A plot of all of the mean cloud emittance-albedo pairs is shown in Fig. 15. The largest concentrations of data are found for $\epsilon_b(T_t) < 0.8$. In general, α_c is greater for a given value of ϵ_b than it is in Fig. 9b. Cloud-top emittance tends to plateau at $\epsilon_b \approx 0.86$, while cloud-center emittance appears to level at $\epsilon_b \approx 0.98$. The lower emittances lead to diminished values of τ_e relative to those derived for T_c.

The emittance ratio, $r_\epsilon = \epsilon_b(T_t)/\epsilon_b(T_c)$, was computed for discrete intervals of T_c. Mean values and standard deviations of these ratios are shown in Fig. 16. The emittance ratio increases almost linearly with decreasing cloud center temperature. Standard deviations about a given mean ratio are less than 0.1. The emittance ratio is close to unity for $T_c < 215$ K.

The well-correlated variation of r_ϵ suggests the possibility that T_t as well as T_c may be retrieved with VIS–IR radiance pairs. This ratio integrates many of the other parameters examined earlier. For example, cloud thickness in Fig. 11 is least at the highest altitudes and increases before leveling or even decreasing for temperatures around 235 K. For the highest clouds, there is little difference between T_c and T_t because the clouds are not very thick. Since cloud depths are greater at lower altitudes, it is possible to sense radiation from areas deep within the cloud thereby causing greater differences between T_c and T_t. As the depth of the cloud decreases, the ratio should approach unity. At higher temperatures ($T_c > 250$ K), the relationship of r_ϵ to T_c may not be as well defined because liquid water becomes more common and the mean cloud depth may not be dependent on T_c. Whether the relationship shown in Fig. 16 is typical for all observing angles is also unknown. Additional sampling from other angles and over a wider variety of temperatures would help to better define the relationship between r_ϵ and T_c. However, the results shown in Figs. 11, 12, and 16 suggest that it may be possible to obtain reasonable estimates of h and T_t over a limited range of T_c.

e. Emittance uncertainties

The parameter values derived here are subject to considerable uncertainty as evidenced by the results in Table 5 and the large standard deviations in earlier figures. Potential sources of error abound in an analysis of this type due to the large number of variables and the nonuniformity of cirrus clouds.

Parameters derived from the lidar essentially provide

TABLE 4. Observed and computed cloud properties for case study ER-2 data.

Day	Time (UTC)	Lat. (°N)	Lon. (°W)	T_s (K)	T_c (K)	h (km)	τ_e	τ_v	ξ	Dark pixel (%)	τ'_v	ξ'
27	1830	45.8	93.1	290.0	225.0	0.5	0.12	0.69	5.73	0	0.46	3.86
	1900	45.3	92.5	288.5	234.0	0.5	0.14	0.51	3.43	0	0.39	2.64
	1930	44.9	91.1	288.4	234.0	0.5	0.24	0.73	2.91	3	0.61	1.68
28	1600	44.6	87.0	283.0	229.0	3.7	0.43	0.86	1.99	0	0.84	1.95
	1600	44.5	87.1	283.0	229.0	3.7	0.42	0.92	2.12	0	0.91	2.10
	1600	44.5	87.1	283.0	229.0	3.7	0.45	1.00	2.21	0	0.99	2.21
	1800	43.6	89.4	288.9	228.0	1.5	0.28	0.90	3.23	0	0.69	2.57

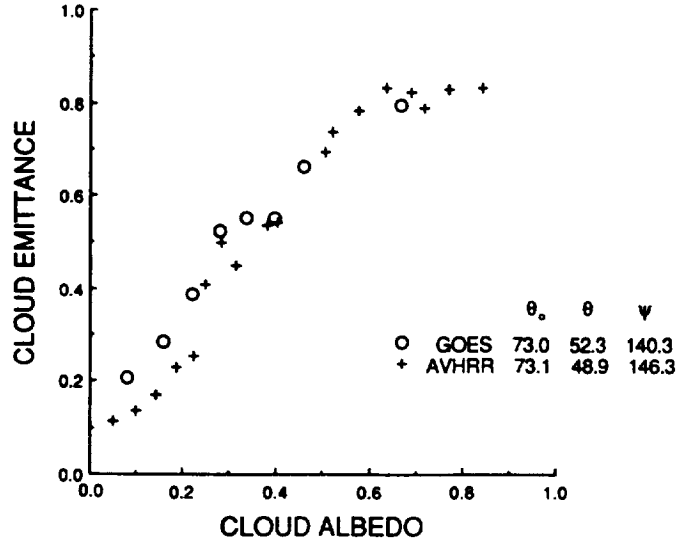

FIG. 13. Comparison of cloud albedos and emittances derived from 28 October 1986 GOES and AVHRR data taken at ~2100 UTC over WAU.

a two-dimensional view of the cirrus clouds. The validity of the assumption that z_c, h, and z_t represent the average cloud heights within the large areas covered by the strip of pixels is difficult to evaluate. One means of estimating how well the lidar data represent the large-area cloud characteristics is to examine the differences between the strip of pixels and surrounding areas. The rms difference between the emittances for the strip and the box containing the strip is 0.05 or 7%. This difference is equivalent to a ±0.7 km variation in cloud-center height between the strip and the box. Changes of 2 km in cloud-center altitude during a given half hour are common as seen in Fig. 1. The variations in the small-scale lidar data are greater than those in the large-scale satellite data as expected.

Assuming that the large-scale differences are representative of the lidar-satellite scale differences, it is estimated that the use of lidar data to set z_c causes an uncertainty in ϵ_a of ±10% based on an average value for ϵ_a of 0.62. Note that no clouds with $\epsilon_b < 0.1$ were included in the analysis because of the cloud-detection threshold of 3 K. A conservative estimate of the uncertainty in T_s is ±2 K. Inclusion of this error raises the overall uncertainty in ϵ_a to ±13%. This uncertainty in ϵ_a is equivalent to a ±20% uncertainty in τ_e for a given scene over the range of optical depths considered here. The AVHRR–GOES comparisons are, on average, within this uncertainty level. The average IR optical thickness is 0.96 for all 71 scenes. From the strip and box comparison, it is also estimated that z_t and h have uncertainties of ±0.7 km.

Another source of uncertainty in ϵ_a is the use of a mean cloud height for the entire scene. This error source may be examined by performing a pixel-by-pixel analysis on a scene that varies systematically with time. One example is the cloud over FMC between 2020 and 2050 UTC. The GOES pixels from the corresponding wind strip data were averaged in lines perpendicular to the wind vector. Using the wind speed, these averaged pixels were converted to times and aligned with the lidar-defined cloud parameters. The results shown in Fig. 17 indicate good alignment between the two datasets. In this case, it appears that the lidar data provide an accurate cross section of the cloud. The GOES reflectance increases as the cloud thickens and T increases as z_c lowers. Equations (1) and (5) were applied to each average pixel using T_c derived from Fig. 17 to determine τ_e and τ_v. Figure 18 shows the variation of the parameters with time. Although the thin part of the cloud is detected with the IR data, a value for τ_v is not computed since the reflectances are lower than that for clear skies. Nevertheless, the mean values for τ_e and ϵ_b derived on a pixel-by-pixel basis are 0.59 and 0.54, respectively, compared to 0.62 and 0.59 derived for the entire scene using a mean value of z_c. This comparison suggests that the error in ϵ_b for using the mean cloud height is around 10% with a slight tendency to bias the values to the high end because of nonlinear effects. While these results may not represent all cases, they indicate that the use of a mean cloud height for the analysis is a reasonable approach.

4. Relationship between VIS and IR parameters

a. Scattering efficiency ratio

For a given cloud particle with cross-sectional area $2\pi a^2$, the VIS scattering cross section is

$$\beta_v = Q_{sca} 2\pi a^2,$$

and the IR absorption cross section is

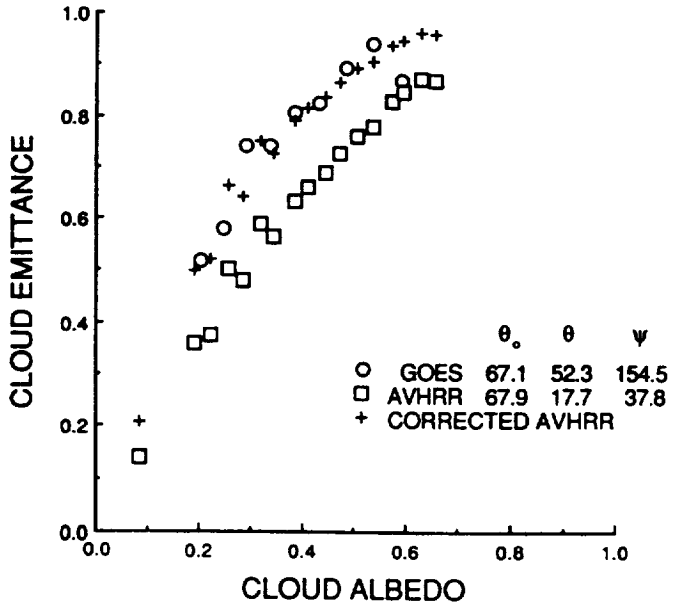

FIG. 14. Same as Fig. 13, except for 2 November 1986 at ~2000 UTC.

TABLE 5. Comparison of AVHRR- and GOES-derived cloud parameters.

		AVHRR Parameters							GOES Parameters						
Site (Day)	T_c (K)	Time (UTC)	Θ (°)	τ_e	τ_v	ξ	ξ'	Dark pixel %	Time (UTC)	τ_e	τ_v	ξ	Dark pixel %	τ_v'	ξ'
FMC															
(28)	231	2100	141	0.83	1.47	1.95	1.96	0	2100	0.72	1.36	1.79	3	1.48	1.94
(30)	223	2042	127	0.25	0.35	1.13	1.79	18	2030	0.17	0.63	3.50	3	0.57	3.12
(2)	230	2006	92	0.49	1.18	1.94	1.36	5	2000	0.39	0.97	2.42	0	0.80	1.98
WAU															
(28)	234	2100	142	0.31	1.69	3.50	21.4	0	2100	0.26	0.78	2.20	6	0.89	2.41
(2)	230	2006	98	1.34	4.61	3.21	1.78	0	2000	1.16	3.26	2.72	0	2.48	2.09

$$\beta_e = Q_{abs} 2\pi a^2,$$

where the VIS scattering efficiency is Q_{sca}, the IR absorption efficiency is Q_{abs}, and the effective particle radius is a. The extinction optical depth for a given wavelength, λ, is

$$\tau(\lambda) = \beta(\lambda) \int N(z)dz,$$

where the integral is over some finite height, β is the extinction optical depth, and $N(z)$ is the number density of particles at z. If it is assumed for a given cloud that the VIS extinction is due entirely to scattering, the IR extinction is due entirely to absorption, and the extinction coefficients are constant, then the scattering-to-absorption ratio is

$$\xi = Q_{sca}/Q_{abs} = \beta_v/\beta_e = \tau_v/\tau_e.$$

Therefore, if ξ and τ_v are known, then the value of τ_e may be determined. This efficiency ratio forms the basis of the ISCCP cloud-height correction algorithm. The values of Q_{sca} and Q_{abs} depend primarily on the particle size in terms of the size parameter, $2\pi a/\lambda$, and the index of refraction. Mie scattering calculations of Q_{sca} and Q_{abs} indicate that ξ for the wavelengths of interest may vary from ~5 for $a = 2.0\ \mu$m to ~2.4 for $a = 10.0\ \mu$m (Sassen 1981). The value of ξ asymptotically approaches 2.0 for very large particles; i.e., $2\pi a/\lambda \gg 1$ (e.g., Hansen and Travis 1974). Platt et al. (1987) have presented some theoretical results that indicate ξ is also a function of particle shape and may have values slightly less than 2.0.

For each satellite-lidar dataset in this study, the scattering efficiency ratio is computed for all of the pixels, N, having a discrete value of ρ as follows.

$$\xi = \sum_{i=1}^{N} (\tau_v/\tau_{e_i})/N. \quad (8)$$

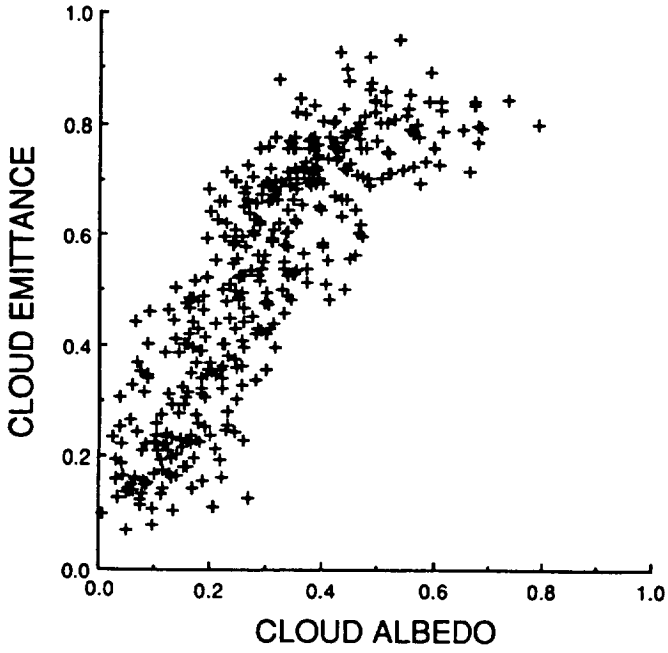

FIG. 15. Same as Fig. 9b, except $T_z = T_c$.

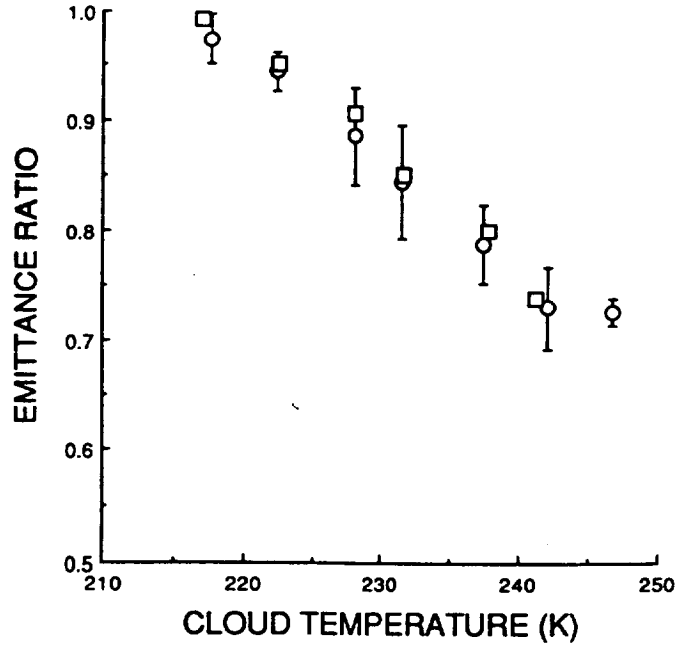

FIG. 16. Variation of ratio of cloud-top emittance to cloud-center emittance on cloud-center temperature for all IFO (circles) and case study (squares) data from GOES over surface lidar sites. Vertical lines denote standard deviations.

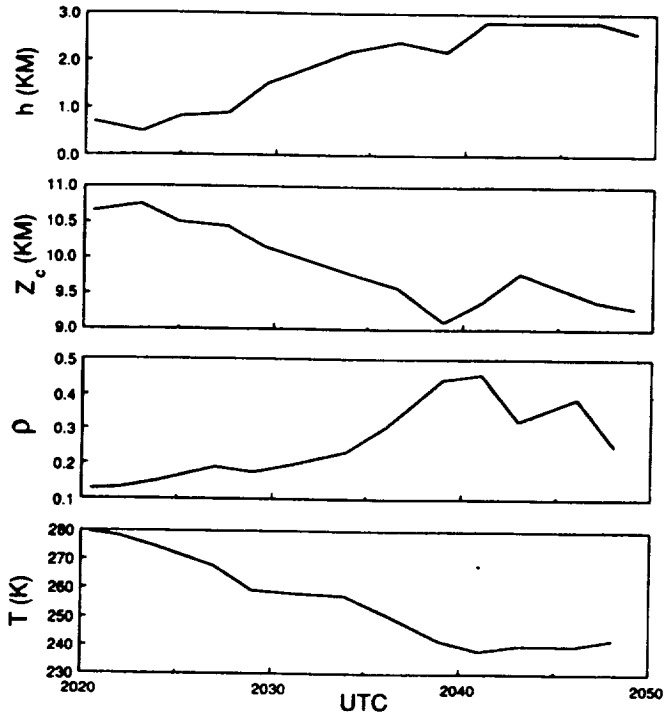

FIG. 17. Comparison of GOES and lidar observations along wind vector over FMC during 28 October 1986.

Only one temperature, T_c, is used to compute τ_e for a given dataset since only one average cloud height is derived for each time. Changes in the actual cloud height and thickness within the scene (e.g., Fig. 1) tend to introduce variations in τ_e for a given reflectance. Thus, the mean value of ξ is computed for each cloud reflectance value to minimize the effects of cloud height variability.

Visible optical depths for the case study GOES data are given in Table 2. Tables 3–5 summarize the results of applying (8) to all of the data. Despite the differences between the values of τ_v for IFO and case study results in Table 3, two similarities are quite evident in a comparison of the respective scattering efficiencies. For both datasets, the scattering efficiency appears to increase with decreasing θ_0 and increasing Θ. At high values of θ_0, ξ is well below the expected limit of 2. The average values of ξ are also very close, 2.17 and 2.13, for the case study and IFO, respectively. In Table 4, the greatest values of ξ also occur near local noon (1800 UTC).

b. *Reanalyzed visible data*

The temporal dependencies of τ_v and ξ are not realistic. They are primarily due to shortcomings in the analysis treatment of χ_c. The anisotropy of the reflected radiation field for real clouds depends on the optical thickness, incident radiation, microphysical properties of the cloud, and the morphology of the cloud field. The value of χ_c used here is fixed for a given set of angles and represents an empirical average for all cloud types. The average cloud optical depth in the bidirectional reflectance model used here is probably close 10, while τ_v for the clouds analyzed in this study generally smaller than 2. Since cirrus clouds are t only type considered here and the angles are fixed f a given hour, it is likely that χ_c will be biased wi respect to local time. There will also be random erro in χ_c due to variations in microphysics, morpholog and cloud optical depth for a given hour. The ma nitudes of these errors are currently unknown, but a potentially large. Assuming that the time samplii represents a random sampling of χ_c, the averages various parameters derived from all times should l relatively unbiased.

Using the assumption that the mean value of ξ independent of time, new values of χ_c were determine from (5) using the observations of τ_e and the mea scattering ratio of 2.13. These new values were average at each time. The means, denoted as χ_c', are given i Table 6 with the mean nominal values from the bid rectional reflectance model. The results indicate mo anisotropy in the cirrus reflectance pattern than in th empirical model. The data of Takano and Liou (1989b indicate that reflectance anisotropy diminishes wit increasing optical depth for scattering by hexagon columns. Thus, the smaller optical depths of the clouc here compared to those for the clouds in the empiric model are probably responsible for the larger range c χ_c' compared to χ_c.

To eliminate the temporal (angular) dependence c τ_v, the data were reanalyzed using χ_c'. The values c the visible optical depth and the scattering ratios de termined from the reanalysis are listed in Tables 2– and denoted with the primed variables, τ_v' and ξ', re spectively. Values of ξ' for the AVHRR data wer computed by changing the nominal values of χ_c so tha the derived value of τ_v' for the AVHRR data was equa to τ_v' for the corresponding GOES data. In general, th

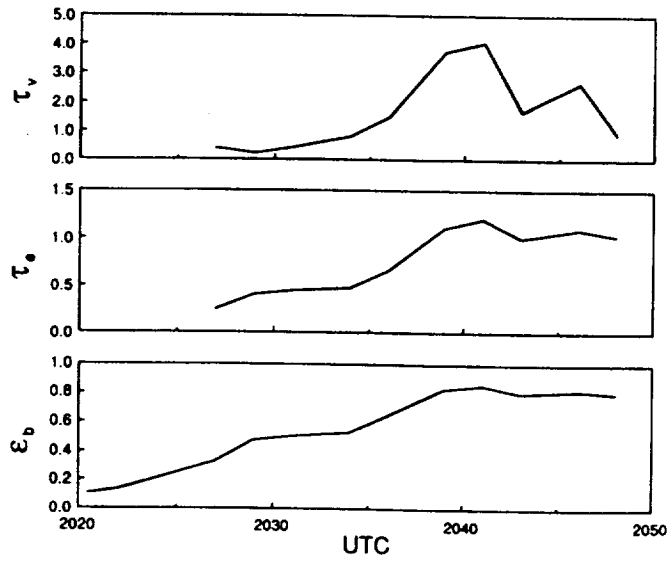

FIG. 18. Cloud optical properties derived from Fig. 17.

TABLE 6. Anisotropic reflectance factor comparison.

Time (UTC)	Number of pixels	χ_c (nominal)	χ_c' ($\xi = 2.13$)	Mean difference	Standard deviation
1330	213	0.823	0.618	0.205	0.104
1400	177	0.864	0.735	0.129	0.050
1430	113	0.896	0.809	0.087	0.113
1500	177	0.922	0.896	0.026	0.079
1600	215	0.980	1.034	−0.054	0.123
1630	146	1.002	0.912	0.090	0.044
1700	212	1.020	1.195	−0.175	0.264
1800	158	1.050	1.206	−0.156	0.348
1830	72	1.061	1.025	0.036	0.000
1900	262	1.029	1.214	−0.185	0.220
1930	236	1.008	1.147	−0.139	0.206
2000	245	0.982	1.091	−0.109	0.164
2030	290	0.953	1.008	−0.055	0.103
2100	222	0.918	0.890	0.028	0.093
2130	283	0.882	0.713	0.069	0.154
2200	210	0.843	0.579	0.264	0.082

new mean optical depths in Tables 2 and 3 have been increased for hours near the terminator and decreased near noon. The temporal dependence of the scattering efficiency ratios has been effectively eliminated for the IFO averages, while some tendency for maximum values near noon remains for the case study results. Resulting means of ξ' are not equal to 2.13 because of the nonlinearities in the solution of (5) and (8) and because four additional scenes were eliminated due to filtering. In Table 4, all of the optical depths and ratios were decreased yielding a mean value for ξ' of 2.43. The new values of χ_c for the AVHRR data (Table 5) reduced the differences between the GOES and AVHRR scattering efficiency ratios with respective means of 2.31 and 2.35 for the five values of ξ'. The greatest difference between the two datasets is found for FMC during 30 October when almost 20% of the AVHRR data are classified as dark pixels.

Mean values of τ_v' were computed for discrete intervals of cloud thickness. The results shown in Fig. 19 reveal a strong, almost linear, dependence of τ_v' on cloud thickness. This apparent relationship lends further support to the potential for deriving cirrus depth from the VIS–IR radiance data. Figure 20 shows the variation of mean ξ' with IR optical depth. The standard deviations of the IFO data are denoted with the vertical lines. The case study averages (squares) vary from 1.79 to 2.54, while the IFO means (circles) range from 1.91 to 2.33. There is good consistency between the IFO and case study results for $\tau_e < 1.0$. Clouds with $\tau_e > 1.0$ were undersampled during the case study (Fig. 9a). These results show no indication of a dependence of ξ' on τ_e.

Average scattering efficiencies were also computed for discrete levels of T_c (Fig. 21). For $T_c > 230$ K, $\xi' \approx 2.0$. Despite the large standard deviations, the mean value of ξ' appears to increase with decreasing temperature for $T_c < 230$ K. At $T_c = 217$ K, the mean

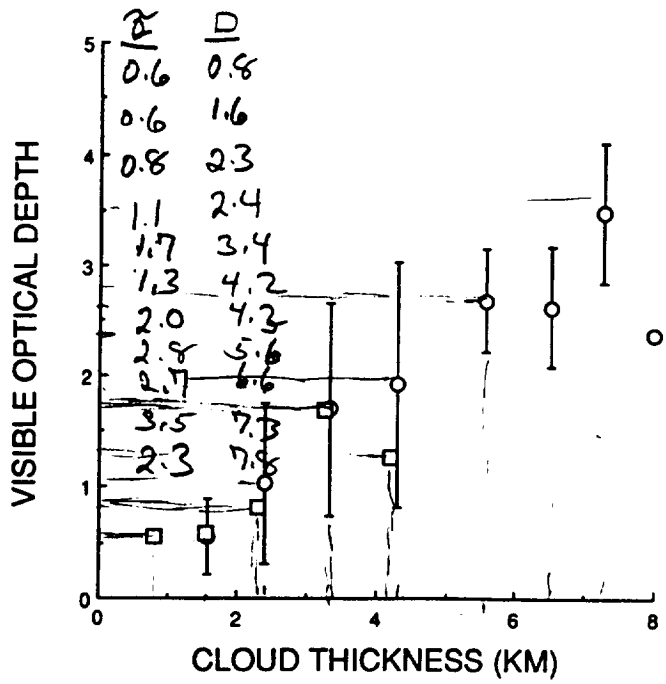

FIG. 19. Variation of cloud visible optical depth with cloud thickness for all IFO (circles) and case study (squares) data from GOES over surface lidar sites. Vertical lines denote standard deviations.

scattering efficiency ratio reaches a maximum of ~2.6 for the IFO data. To determine if there is a significant difference between the results for cold and warm cirrus clouds, average values for ξ' were computed for $T_c \leq 230$ K and for $T_c > 230$ K. For the thirty cases with $T_c \leq 230$ K (cold clouds), the mean value of ξ', $\overline{\xi'}$ is 2.43 with a standard deviation of 0.89. For the other

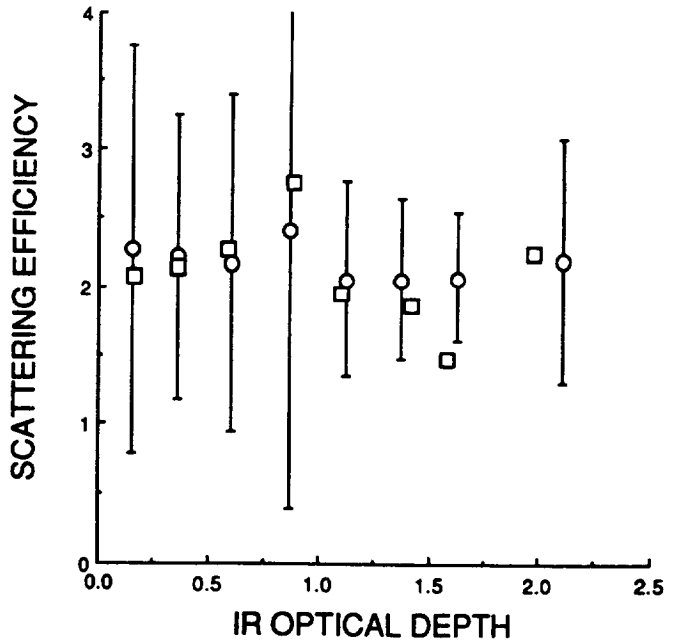

FIG. 20. Variation of mean scattering efficiency ratio with infrared optical depth for all IFO (circles) and case study (squares) data from GOES over surface lidar sites. Standard deviations denoted by vertical lines.

37 scenes (warm clouds), the mean scattering efficiency ratio is 2.11 with a standard deviation of 0.71. Application of sampling theory with an assumption of normal distributions yields $\bar{\xi}' = 2.43 \pm 0.17$ for the cold clouds and $\bar{\xi}' = 2.11 \pm 0.12$ for the warm clouds. (The mean for all 67 cases, 2.25, differs from that in Table 3 because of different averaging techniques.) Using a two-tailed Student t-test, it was found that the cold-cloud ($T_c \leq 230$ K) ratios are different from the warm-cloud values at the 90% confidence level. The mean ratio for the warm clouds is not significantly different from 2.0, the lower limit expected for large particles.

As noted earlier, the value of ξ is highly dependent on the particle size. Neglecting the effects of particle shape, it may be concluded from these results that large particles are the dominant scatterers in the clouds for $T_c > 230$ K. At colder cloud temperatures, smaller particles (e.g., $a < 20$ μm) apparently contribute more to the scattering. Thus, the average particle size in the colder clouds must be significantly less than the warmer clouds. Figure 21 suggests that the proportion of small particles in the clouds increases as the cloud-center temperature decreases. These findings are consistent with the results of Platt and Dilley (1981) who determined that the lidar-measured backscatter-to-extinction ratio is relatively constant for $T_c > 233$ K. The value of that ratio changes abruptly to a new value at temperatures slightly less than 233 K. Heymsfield and Platt (1984) were able to show that the number density of large particles in cirrus clouds decreased substantially when the temperature dropped below −40°C. The VIS extinction coefficients derived from the GOES data are

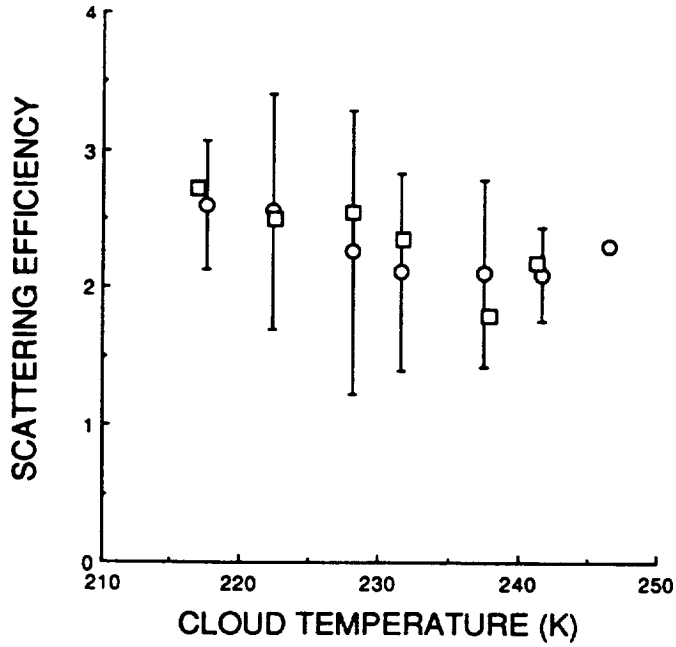

FIG. 21. Variation of mean scattering efficiency ratio with cloud-center temperature for all IFO (circles) and case study (squares) data from GOES over surface lidar sites. Vertical lines denote standard deviations.

0.41 km^{-1} and 0.45 km^{-1} for $T_c \leq 230$ K and $T_c > 230$ K, respectively. These values fall in the range of values computed by Heymsfield and Platt (1984), but show less dependence on temperature.

Although particle size is very important in the determination of ξ, Platt et al. (1987) have presented theoretical results indicating that ξ is also a function of particle shape. The results of Heymsfield and Platt (1984) show that ice crystal habits change significantly when the cloud temperature drops below 233 K. Thus, both factors, smaller crystals and shape changes, may explain the increase in ξ for $T_c < 230$ K observed in the current dataset. Microphysical measurements using probes sensitive to small ice particles are needed to further clarify these results.

c. *Assumptions for visible optical depth calculations*

The determination of τ_v' relies on the assumptions that the clouds can be modeled as plane parallel entities, that (5) is an adequate parameterization of a more exact radiative transfer model, and that the cloud albedo model, or the implied scattering phase function, is appropriate for the clouds studied here. The lidar plots in Figs. 1 and 2 show considerable structure in the clouds observed during 28 October. Such morphology is probably typical of most of the cirrus clouds observed during the IFO. Thus, the clouds do not appear to be plane-parallel and homogeneous. Because exact modeling of the nonhomogeneous clouds is not possible at this time, no attempt is made to estimate the effects of cloud morphology on the derived values of VIS optical depth.

One means of evaluating the parameterization is to compare the results of (5) with values of τ_v derived for each scene with a detailed radiative transfer model using the scattering phase function that produced the cloud albedo model applied in (5). Takano et al. (1989) computed τ_v for several of the IFO scenes using a three-level adding–doubling radiative transfer model with two different scattering phase functions. One of the phase functions was the same as that used to derive the cloud albedo model employed here. The other was for ice spheres with areas equivalent to the hexagonal columns used in the first phase function. Takano et al. (1989) used a Lambertian surface with an albedo of 0.11 to simulate the Wisconsin land areas. They determined the value of τ_v for 16 scenes during the case study period by matching the reflectance of the adding-doubling model at the GOES angles to the mean GOES-derived reflectance of the square area around each lidar site. The pixels in the same areas (which include the strips analyzed earlier) were analyzed with the parameterization using the values of χ_c'.

A comparison of the results showed that the average value of τ_v for the radiative transfer model using hexagonal crystals was 0.95 compared to an average of 0.99 for the parameterization. The rms difference was

17%. Although the 0.04 mean difference is not statistically significant, it is expected for several reasons. The Takano et al. (1989) results include all of the pixels in the region, while the results from (5) exclude all dark pixels. Furthermore, the radiative transfer model does not include ozone absorption. Exclusion of the dark pixels and inclusion of ozone absorption would both tend to increase the mean model-derived optical depth by a few percent. The rms differences are most likely due to the use of a Lambertian surface albedo in the adding–doubling model and the use of a fixed value of χ_c' for each hour in (5). The mean value of ξ for the model results was 2.55 compared to 2.56 for the parameterization. From these comparisons it is evident that (5) is quite adequate for parameterizing the detailed radiative transfer model for the range of optical depths seen in the case study. In addition, the good agreement between the average derived values of ξ' over land and water at the same hour (i.e., 1600 UTC) in Table 4 indicates that (5) is useful over a reasonable range of surface albedos.

The cirrus clouds observed during the IFO contained mixtures of hexagonal columns, plates, and aggregates of various sizes and shapes (Kajikawa and Heymsfield 1989). Even water droplets were found in some of the warmer cirrus clouds (Sassen et al. 1990). In this study, the visible radiances have been treated as if they were reflected from a cloud composed entirely of one size of hexagonal columns. Although exact evaluation of the uncertainty in τ_v due to the use of the single phase function is not possible, some inferences may be drawn from the results to make a qualitative assessment of the hexagonal column, cloud-albedo model.

One indication of the reasonability of the model used here is that the mean value of ξ is close to the limit of 2.0 expected for large particles, especially for the warmer clouds. An examination of the results of Takano et al. (1989) reveal that the mean value of τ_v derived with the equivalent ice-sphere model was 30% greater than that for the hexagonal column model. The resulting mean value of ξ for the ice spheres is 2.9. These results indicate that the ice-crystal model is more appropriate than the spherical model for interpreting the cirrus reflectance data.

The adding–doubling model of Takano and Liou (1989b) was used to calculate the cloud reflectances for the angles corresponding to GOES and AVHRR in Table 5 using the values of τ_v' and the hexagonal column phase function. The resulting reflectances at the GOES angles were ratioed to the corresponding reflectances at the AVHRR angles. For the three cases in which the GOES and AVHRR angles differed significantly (30 October and 2 November), the average ratio for the adding–doubling results was 1.6 compared to 1.3, the mean ratio of the GOES and AVHRR values of χ_c'. About half of the difference in the mean ratios may be due to the uncertainties in the values of χ_c' for each individual case. Thus, the actual difference in the ratios may be as small as 0.15. This limited result suggests that the actual scattering by the cirrus clouds may be less anisotropic than expected for the hexagonal crystal model. Although discrepancies between the microphysical characteristics of the actual and modeled clouds are likely to cause differences between the observed and modeled radiation fields, some of the tendency for more diffuse reflectance from the cirrus may be due to shadowing effects as discussed below. A more complete analysis using much more data is required to better define typical cirrus reflectance anisotropy and the single scattering phase function that accounts for it. Given the current knowledge of cirrus cloud radiative properties, however, the cloud albedo model used in (5) appears to be adequate for computing τ_v'.

d. Dark pixels

It is possible that the "dark" pixels noted earlier may be caused by the extreme reflectance anisotropy expected for very thin clouds. For small values of τ_v and $\Theta \sim 120°$, there should be very little reflection from the cloud in the direction of the satellite as compared with its albedo to upwelling diffuse radiation from the surface. Thus, the pixel may appear darker than a clear scene for the same viewing and illumination conditions.

Examples of the variations of ρ as a function of α_c computed with (5) are shown in Fig. 22a for WAU at 1400 and 1800 UTC. The corresponding values of ρ_s are 0.13 and 0.16, respectively, with $\alpha_{sd} = 0.11$. The relationship between cloud albedo and optical depth depends on the solar zenith angle resulting in a divergence of the curves at larger values of α_c. Additional calculations were performed for $\mu_0 = 0.4$; $\chi_c = 1$; and $\rho_s = 0.04, 0.08, 0.16, 0.32$, and 0.64; with $\alpha_{sd} = 0.92\rho_s$.

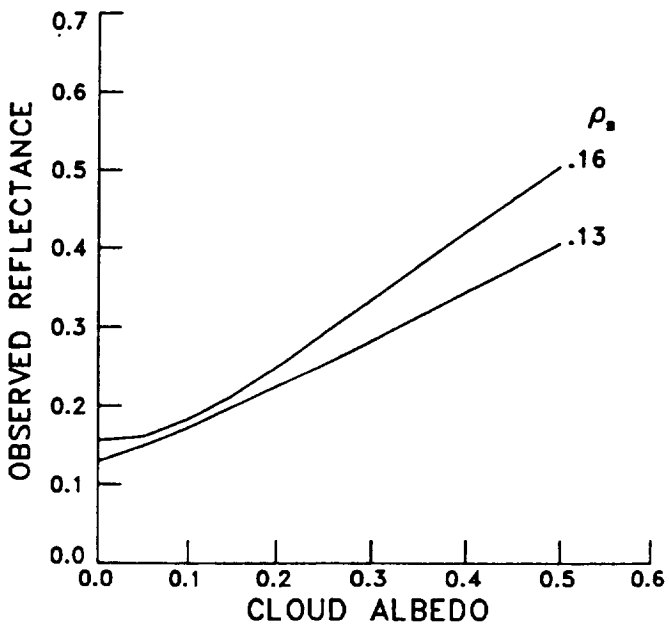

FIG. 22a. Theoretical top-of-the-atmosphere visible reflectance over WAU for 1400 UTC ($\rho_s = 0.13$) and for 1800 UTC ($\rho_s = 0.16$).

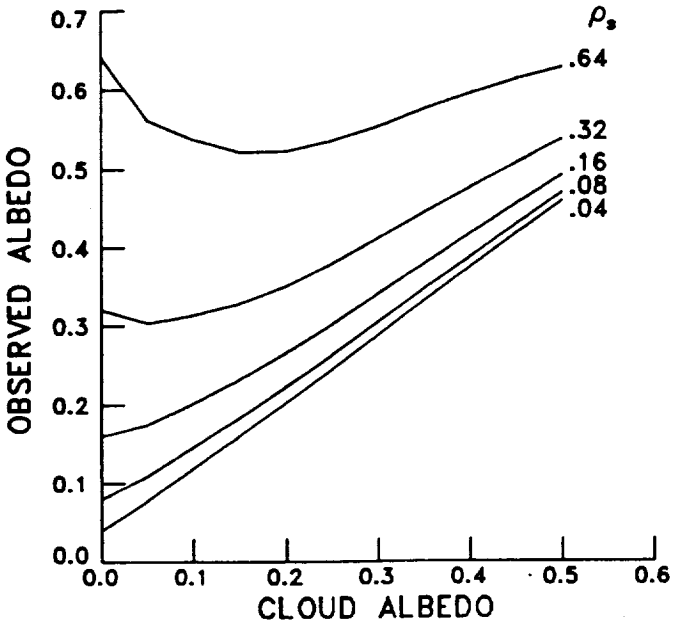

FIG. 22b. Theoretical top-of-the-atmosphere visible albedos for various surface albedos.

The results are shown in Fig. 22b. For relatively dark surfaces, the measured reflectance increases monotonically with α_c. Over bright surfaces, the reflectance actually decreases first, then increases at greater cloud albedos. A dark surface contributes little to the upward flux, while the opposite is true for bright surfaces. The increased reflectance of a cloud to diffuse radiation tends to trap some of the reflected radiation from the surface. For thin clouds over bright surfaces, this effect can result in a reflectance that is lower than that observed for the clear-sky case. Additional calculations for other solar zenith angles indicate that the insertion of the thin cirrus cloud above the bright surface decreases the albedo at lower sun angles, making the discrimination of clear and cloudy skies more difficult over deserts and other bright scenes. It is possible that this effect may also be important at certain angles and values of χ_c over dark surfaces.

Although such a mechanism may cause some pixel darkening, it is probably not the primary cause. Cloud shading is more likely to be the predominant cause of dark pixels. For example, at altitudes of 10 km, a 2 km thick cloud can cast a shadow that has its leading edge removed at least 8 km horizontally on the surface from the position of the cloud's leading edge for $\theta_0 \geq 45°$. Thus, the cloud and the portion of the surface affected by direct transmission through the cloud can easily be offset by one or more GOES pixels. The projected line of sight from the satellite through a cloud will not line up with the cloud's shadow unless $\Theta \approx 180°$. In most instances, therefore, the direct transmission from the surface through the viewed cloud will come from the shadow of a different cloud. The diffuse reflectance will result from the combined effects of the various clouds in the vicinity. For a homogeneous cloud field, an optically thick viewed cloud, or $\Theta = 180°$, such effects are negligible. Figures 1, 2, and 17 provide ample evidence that the clouds observed during the case study are neither optically thick nor homogeneous. In an inhomogeneous cloud field, it is possible to observe a surface darkened by the shadow of a thick cloud through a thin cloud that produces little scattering of its own in the direction of the satellite. Thus, to the viewer in space a pixel appears to be a cloud by virtue of its cold temperature, but is darker than expected for a clear scene.

This effect may be examined quantitatively by considering (5). Use of that model implicitly assumes a homogeneous cloud field. To consider an inhomogeneous cloud field, let τ_s replace τ_v in (6), where τ_s is the VIS optical depth of the cloud casting a shadow onto the surface in the line of sight of the observed cloud that has optical depth τ_v. Since the diffuse radiation emerging from the bottom of the clouds and reflecting from the surface is coming from all of the clouds in the field, let α_c in the third term of (5) be replaced by the average albedo of the observed and the shading cloud. The results of solving this inhomogeneous version of (5) for two different observed clouds are displayed in Fig. 23. The circles represent $\tau_s = \tau_v$. Viewing angles were fixed at $\theta = 52°$ and χ_c varied with θ_0, which changed with time as in the lower halves of Tables 3 and 6. Clear-sky reflectance is denoted with the dashed horizontal line.

The greatest effects of cloud inhomogeneities are seen for $\tau_v = 0.25$. Both shading clouds cause dark pixels for $\theta_0 < 81°$. Some dark pixels occur for $\tau_s = \tau_v$ for $\theta_0 < 60°$. Calculations using smaller μ_0's produced no dark pixels. The thickness of the shading cloud becomes more important as μ_0 increases. The impact of shading on the observed cloud having $\tau_v = 1$ is less pronounced with little likelihood of dark pixels for the range of μ_0

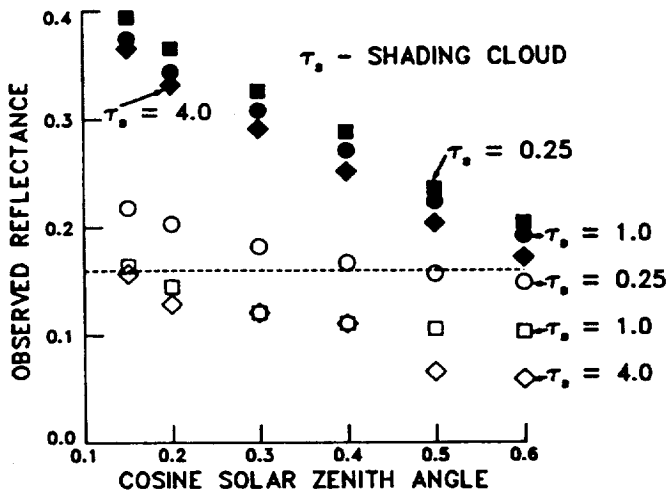

FIG. 23. Effect of cloud shading on observed reflectance. Optical depth of observed cloud is τ_v. Solid symbols, $\tau_v = 1$. Open symbols, $\tau_v = 0.25$. Dashed line is clear-sky reflectance.

considered. Shading by the thin cloud ($\tau_s = 0.25$) actually increases the observed reflectance for all cases using $\tau_v = 1$. As τ_v increases to larger values, the impact of τ_s will become negligible. This lack of a shadowing effect for thicker clouds suggests that the observed reflectance may be biased toward a value that is lower than expected when the scene contains both optically thick ($\tau_v \geq 2$) and thin clouds, even if no dark pixels occur.

Shadowing effects can be observed in the data shown in Fig. 18. Dark pixels corresponding to the thinnest part of the cloud are seen before 2027 UTC. The next few pixels to the right are detectable but τ_v is much less than τ_e. The VIS optical depth for the pixels corresponding 2040 UTC is more than three times the value of τ_e, suggesting enhanced reflectance. In this figure, the sun would be located approximately to the right of the figure at $\theta_0 = 68°$. With a cloud top near 11 km, the thickest part of the cloud would cast a shadow approximately 28 km to the left or to the position corresponding to 2025 UTC. The view from the satellite is at a 35° angle, not perpendicular, to the solar plane. Thus, the surface in the line of sight of the cloud at 2025 UTC would correspond to the 2020 UTC position. That surface would be shaded by a cloud with $\tau_e \approx 0.5$ or $\tau_v \approx 1.0$ assuming that Fig. 18 is an accurate cross section of the cloud. A dark pixel would be expected at 2020 UTC based on the results in Fig. 23. The first visibly detectable cloud coincides with $\tau_e \approx 0.3$ at 2027 UTC. Its value of τ_v is much less than the expected value of 0.6.

While the shading can explain the darker pixels, it does not account for the excessively bright ones at 2040 UTC. For these bright pixels, it is instructive to refer to the cloud structure in Fig. 1. The vertical thickness of the cloud changes rapidly so that the pathlength of the incident solar radiation through the cloud is not necessarily $h\sec\theta_0$. The pathlength may be substantially increased because of the cloud structure. For example, the sun angle may coincide with the right arm of the "V" defining the cloud centered at 2035 UTC in Fig. 1. This effect would tend to cause a cloud to appear brighter than expected for the observed τ_e. In this case, the shadowing and enhancement effects apparently cancel to yield a reasonable value of ξ' for the whole scene.

The occurrence of dark pixels is shown in Fig. 24 as a function of ϵ_b. Most of the dark pixels are found at emittances corresponding to $\tau_e < 0.2$. Some, however, are found for $\tau_e = 0.5$. Very few dark pixels were observed near noon when $\Theta > 160°$. Most were found in the midmorning and late afternoon when shading conditions were favorable. The dark pixels comprise only 3% of the data considered here. This percentage belies the importance of this effect since shading will occur in many instances without producing the easily detectable dark pixels. The shading effect will tend to reduce the observed reflectance causing an underestimation of the cloud's thickness and emittance. Cloud shadows or their absence will also affect the interpretation of reflectance anisotropy. Their presence at high solar zenith angles will yield lower than normal values of τ_v.

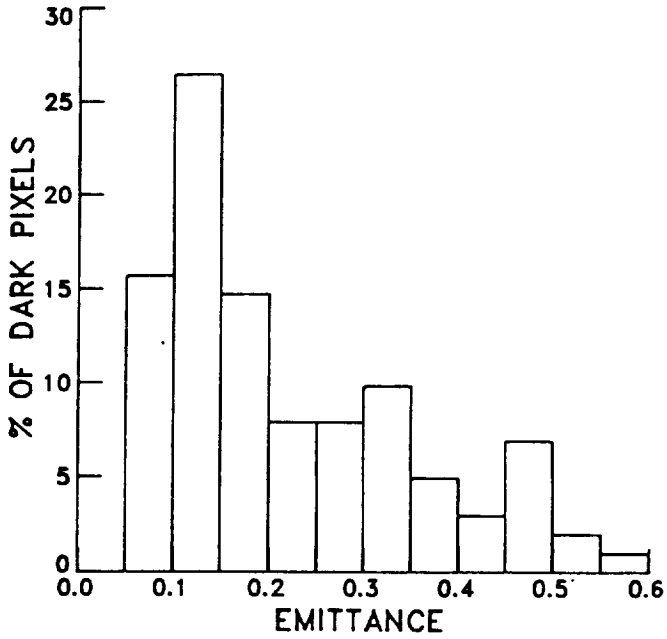

FIG. 24. Percentage of total number of "dark" pixels as a function of effective beam emittance, ϵ_b.

5. Conclusion

The cirrus clouds observed during the case study days are similar to those observed in previous research. By comparison, however, they are not necessarily typical of midlatitude cirrus clouds since their bulk properties are significantly different from those observed during other IFO cirrus days.

The analysis performed in this study using a combination of ground-based and satellite instrumentation yields some results that are similar to earlier studies that utilized other combinations of platforms and instruments. This consistency of results for different approaches lends a higher degree of confidence to the common findings. In addition, the combined datasets used here have provided some valuable new insights into the problem of determining cirrus cloud properties using VIS and IR radiance pairs from satellites.

The determination of cloud-top emittance or actual cloud-top temperature appears to be feasible based on the results of this study. Previously, what has been termed cloud-top temperature in emittance-adjusted, VIS-IR retrievals is closer to cloud-center temperature. The emittance ratio and the dependence of cloud thickness on cloud-center temperature derived here may be utilized in a scheme to estimate cloud thickness. This latter parameter will be useful for computing radiative divergence for observed cirrus clouds.

The results indicate that scattering efficiencies are greater for colder clouds. This finding holds promise for improvements in determining the IR optical depth from reflected VIS data. Additional study, however, is required to confirm this conclusion.

From the examination of the reflectance data and scattering efficiencies it is concluded that much work remains to adequately describe the scattered radiation field for real cirrus clouds. Both theoretical and empirical bidirectional reflectance models should be developed for clouds composed of realistic particle shapes. As in the ISCCP model, the patterns should be developed for various optical depths. Those models will require confirmation with the aid of further observational data. The effects of cloud particle scattering in IR radiative transfer should also be examined observationally.

Cloud shadows are a problem for the interpretation of cloud reflectances, especially for cirrus. The effects are not limited to large solar zenith angles. Relatively high viewing zenith angles can produce situations that result in the viewing of shadows, even for the near-zenith sun. It is apparent that analysis of a single pixel is most sensitive to shadowing problems. Some of the effects may be diminished through averaging over several pixels. Other approaches to deal with shading need to be developed. Validations of cirrus scattering calculations must also consider these effects. The problem of shadows is not as important over water because of the low surface albedo. Other problems in remote sensing of clouds such as partially cloud-filled pixels have not been considered here. Future research efforts should address these other factors.

Acknowledgments. The contributions of Messrs. P. Heck, R. Wheeler, and G. Gibson of Lockheed Engineering and Sciences Company to the satellite data reduction and graphics are deeply appreciated. We also thank Ms. S. Morgan of Computer Sciences Corporation for her assistance in reducing the GOES data. Discussions with Dr. B. A. Wielicki of NASA Langley Research Center were also quite helpful. We would also like to thank Drs. K. N. Liou and Y. Takano of the University of Utah for making their radiative transfer model available. The Madison lidar measurements were supported by ARO Grant DAAG29-84-K-0069, ONR Grant N00014-87-K-0436, and NASA Grant NAAG1-882.

APPENDIX A

Low and thick cloud filtering

The presence of low clouds contaminates the data since the analysis is predicated on the presence of only one cloud layer (the cirrus layer may contain two or more distinct sublayers). The cloud heights are defined for the upper-level cloud (generally, $z_b > 4$ km) detected by the lidar. In some instances, the occurrence of low clouds was either noted by the lidar operators or evident in the backscatter intensity plots. In other cases, the visual observations were not recorded or the low clouds were located within the satellite-defined area around the site, but beyond the observer's horizon. The datasets containing low clouds must either be eliminated or the pixels contaminated by low clouds must be removed. Elimination of all datasets containing low clouds would substantially reduce the number of samples.

In order to define a simple preprocessing filter, it is first assumed that $\alpha_c \propto \tau_v$ for small optical depths. It is also assumed that, to a first approximation, $\rho = T_a\alpha_c + \rho_s(1 - \alpha_c)^2$ and $\alpha_c = \rho_c$. Using the definition of ξ (§ 3e) and (4), it can be shown that

$$\epsilon_b = 1 - \exp(-k\alpha_c/\mu), \tag{7}$$

where k is the constant of proportionality. Values for k are determined in the following manner. For a given site and time, ϵ_b is computed with (1) for each cloudy pixel having $D > D_s$ and $T < T_s - 3$ K. The mean emittance is then computed for each value of D corresponding to the approximated value of α_c. Equation (7) is solved for k using each albedo-emittance pair. An average value of k is then computed for a specified subset of the data. This procedure is applied using $T_z = T_c$.

To filter the data, it is assumed that low clouds are generally brighter than cirrus, but their emittances depend on albedo, as in (7), in the same manner as cirrus. Thus, if a maximum cloud albedo is known for a given cirrus emittance, then it may be assumed that any pixels brighter than that maximum contain some low clouds. The values of those maximum albedos, α_{max}, must be estimated here. To determine those maximum values, the histograms were first filtered manually to obtain a set containing no low clouds. The maximum albedo for each temperature (emittance) was extracted for every histogram at a given time. Data taken on 22 October 1986, were used in the analysis. All maxima for a given time were compared to determine the greatest values for that time. Very little dependence on time was found in this comparison. Therefore, the maxima from all hours were combined. The resultant values were then used to solve (7) for k using a least-squares regression fit. The results were averaged to obtain the coefficient, k_{max}, which is used to define the maximum cloud albedo for a given emittance. The results of this process yield $k_{max} = 2.4$. Thus, for a given time, (7) may be solved for α_{max} using k_{max} and the emittance. Any pixel with $\alpha_c > \alpha_{max} + 0.025$ is assumed to contain low clouds and is eliminated from further processing. The 0.025 increment is an estimate of the uncertainty in α_{max} resulting from the use of an approximation.

An example of this filtering is shown in Fig. A1 for the data over FMC at 1930 UTC 28 October when low clouds were noted in the observer's log. Crosses represent individual pixels. The solid line represents α_{max}

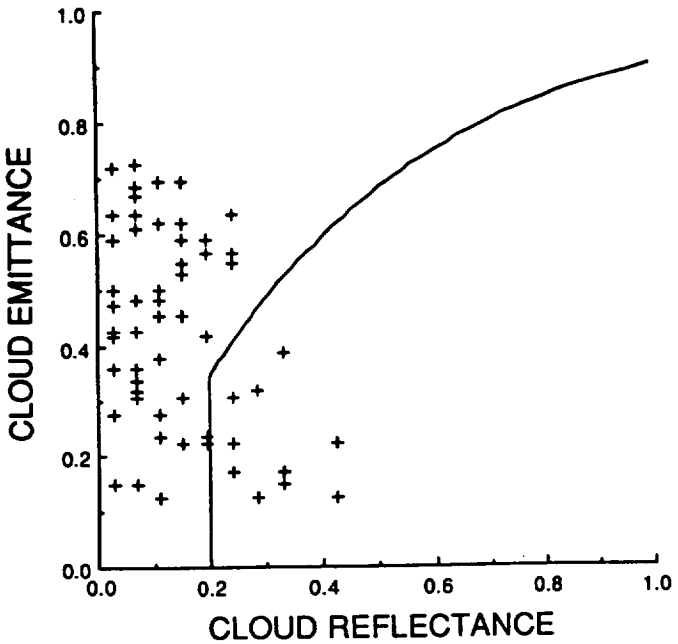

FIG. A1. Example of low-cloud filter application over FMC at 1930 UTC 28 October 1986. All data to right of solid line correspond to low clouds.

computed using k_{max}. The vertical line, $\alpha_{max} = 0.20$, is used at low reflectances because of larger uncertainties at those reflectance levels. This value is based on a visual inspection of the data that contained low clouds. The filtering process eliminates the pixels that clearly contain low clouds (i.e., those to the right of the line). Some pixels containing both low and high clouds, however, may remain in the data.

All cases having $\tau_v > 5.0$ were also removed from the dataset. This arbitrary limit was imposed to minimize the uncertainties in τ_e, τ_v, and subsequent values of ξ. The absolute error in derived optical depth increases with increasing emittance. The value of T_c is also more uncertain for thick clouds than thinner clouds. Thus, errors in emittance are greater for these thick clouds. Their removal does not significantly affect the trends in the results. Inclusion of the thick clouds, however, greatly increases the noise in the data. No case study scenes were affected by the thick-cloud elimination.

APPENDIX B

Partially cloud-filled pixels

The use of (7) or (8) implicitly assumes that the pixel is completely filled with cloud. While it is likely that some of the pixels are partially clear, definitive means for determining which are overcast and which are partly cloudy are unavailable. Platt (1. .., ...posed a bispectral method to discriminate partly cloudy pixels from those containing thin clouds. His technique requires uniform blocks of constant height and thickness for detection of partly cloudy pixels. Detection of thin clouds allows variable thicknesses, but not heights. As seen in Figs. 1 and 2, real cirrus clouds are anything but uniform and constant in altitude and depth. An actual cloud field may also contain broken clouds with variable optical depths. The nonuniformity of such real clouds blurs the distinction between the linear relationship for partly cloudy pixels and the exponential dependency for variable thickness overcast pixels. Over land the ISCCP algorithm uses a threshold of 6 K colder than the clear-sky temperature to determine cloudy pixels (Rossow et al. 1988). Because of the low spatial variability in T_s over the land areas in this study, it is assumed here that pixels colder than $T_s - 3$ K are overcast. The data are not used, however, if there is evidence of any significant breaks in the ceiling from the lidar displays or if the mean IR optical depth is less than 0.1. Very few breaks were seen over the sites on 28 October. The cirrus observed on 27 October were mostly scattered leading to the selection of only two scenes for that day.

APPENDIX C

List of symbols

a	particle radius
B	Planck function at 11.5 μm
D, D_s	observed and clear-sky visible counts
h	cloud thickness
k, k_{max}	albedo coefficient, albedo coefficient for maximum cloud albedo
Q_{abs}, Q_{sca}	absorption and scattering efficiencies
r_e	cloud-top and -center emittance ratio
T, T_s	observed and clear-sky 11.5 μm equivalent blackbody temperatures
T_c, T_t	cloud-center and -top 11.5 μm equivalent blackbody temperatures
T_a	clear-sky temperature estimated from surface data
T_z, T_g	air temperatures at altitude z and at the surface
t	time
u	ozone abundance
z_b, z_c, z_t	cloud-base, cloud-center, and cloud-top altitudes
α_c, α_d	cloud and diffuse cloud albedos
α_s, α_{sd}	clear-sky albedo, clear-sky diffuse albedo
α_{max}	maximum albedo for high clouds at a given emittance
β, β_v, β_e	extinction, scattering, and absorption cross sections
γ	density of particles in the medium
ϵ_a, ϵ_b	vertical emittance, beam emittance
Θ	single-scattering angle
θ, θ_0	viewing zenith angle, solar zenith angle
λ	latitude or wavelength
μ, μ_0	$\cos\theta$, $\cos\theta_0$
ξ	scattering efficiency ratio
ρ, ρ_s, ρ_c	observed, clear-sky, and cloud visible reflectance
σ	volume extinction coefficient

τ_e, τ_v	infrared absorption and visible scattering optical depths
τ_s	visible scattering optical depth of shading cloud
T_a, T_c, T_u	ozone, downward cloud, and upward cloud transmittances
ϕ	longitude
χ_s, χ_c	clear-sky and cloud anisotropic reflectance factors
ψ	relative azimuth angle
IFO	Intensive Field Observations (19 October–2 November 1986)
IR	infrared window (11.5 μm)
FMC	Ft. McCoy, Wisconsin
UTC	Coordinated Universal Time
MAD	Madison, Wisconsin
WAU	Wausau, Wisconsin
VIS	visible (0.65 μm)

REFERENCES

Grund, C. J., and E. W. Eloranta, 1990: The 27–28 October 1986 FIRE IFO cirrus case study: optical properties of cirrus clouds measured by the high spectral resolution lidar. *Mon. Wea. Rev.*, **118**, 2344–2355.

Hahn, C. J., S. G. Warren and J. London, 1988: Surface synoptic cloud reports for Wisconsin, 86 Oct–Nov 3. Cooperative Inst. for Research in Environ. Sci., Campus Box 449, Univ. of Colorado, Boulder, CO, 15 pp.

Hansen, J. E., and L. D. Travis, 1974: Light scattering in planetary atmospheres. *Space Sci. Rev.*, **16**, 527–610.

Heymsfield, A. J., and C. M. R. Platt, 1984: A parameterization of the particle size spectrum of ice clouds in terms of the ambient temperature and the ice water content. *J. Atmos. Sci.*, **41**, 846–855.

Kajikawa, M., and A. J. Heymsfield, 1989: Aggregation of ice crystals in cirrus. *J. Atmos. Sci.*, **46**, 3108–3121.

Liou, K. N., 1973: Transfer of solar irradiance through cirrus cloud layers. *J. Geophys. Res.*, **78**, 1409–1418.

——, 1986: Influence of cirrus clouds on weather and climate processes: a global perspective. *Mon. Wea. Rev.*, **114**, 1167–1199.

——, and G. D. Wittman, 1979: Parameterization of the radiative properties of clouds. *J. Atmos. Sci.*, **36**, 1261–1273.

McClatchey, R. A., R. W. Fenn, J. E. A. Selby, F. E. Volz and J. S. Garing, 1973: Optical properties of the atmosphere (3rd edition). AFCGRL-72-0497, 113 pp. [NTIS-N73-18412.]

Minnis, P., and E. F. Harrison, 1984a: Diurnal variability of regional cloud and clear-sky radiative parameters derived from GOES data, Part I: analysis method. *J. Climate Appl. Meteor.*, **23**, 993–1011.

——, and ——, 1984b: Diurnal variability of regional cloud and clear-sky radiative parameters derived from GOES data, Part III: November 1978 radiative parameters. *J. Climate Appl. Meteor.*, **23**, 1032–1051.

——, E. F. Harrison and G. G. Gibson, 1987: Cloud cover over the eastern equatorial Pacific derived from July 1983 ISCCP data using a hybrid bispectral threshold method. *J. Geophys. Res.*, **92**, 4051–4073.

——, P. W. Heck and E. F. Harrison, 1990: The 27–28 October 1986 FIRE Cirrus IFO case study: cloud parameter fields derived from satellite data. *Mon. Wea. Rev.*, **118**, 2426–2446.

Paltridge, G. W., and C. M. R. Platt, 1981: Aircraft measurements of solar and infrared radiation and the microphysics of cirrus cloud. *Quart. J. Roy. Meteor. Soc.*, **107**, 367–380.

Platt, C. M. R., 1973: Lidar and radiometric observations of cirrus clouds. *J. Atmos. Sci.*, **30**, 1191–1204.

——, 1979: Remote sounding of high clouds, I: calculations of visible and infrared optical properties from lidar and radiometer measurements. *J. Appl. Meteor.*, **18**, 1130–1143.

——, 1983: On the bispectral method for cloud parameter determination from satellite VISSR data: separating broken cloud and semitransparent cloud. *J. Climate Appl. Meteor.*, **22**, 429–439.

——, and A. C. Dilley, 1979: Remote sounding of high clouds: II. Emissivity of cirrostratus. *J. Appl. Meteor.*, **18**, 1144–1150.

——, and G. L. Stephens, 1980: The interpretation of remotely sensed high cloud emittances. *J. Atmos. Sci.*, **37**, 2314–2322.

——, and A. C. Dilley, 1981: Remote sounding of high clouds: IV. Observed temperature variations in cirrus optical properties. *J. Atmos. Sci.*, **38**, 1069–1082.

——, and ——, 1984: Determination of cirrus particle single-scattering phase function from lidar and solar radiometric data. *Appl. Opt.*, **23**, 380–386.

——, D. W. Reynolds and N. L. Abshire, 1980: Satellite and lidar observations of the albedo, emittance, and optical depth of cirrus compared to model calculations. *Mon. Wea. Rev.*, **108**, 195–204.

——, J. C. Scott and A. C. Dilley, 1987: Remote sounding of high clouds, VI. Optical properties of midlatitude and tropical cirrus. *J. Atmos. Sci.*, **44**, 729–747.

Reynolds, D. W., and T. H. Vonder Haar, 1977: A bispectral method for cloud parameter determination. *Mon. Wea. Rev.*, **105**, 446–457.

Rossow, W. B., L. C. Garder, P. Lu and A. Walker, 1988: International Satellite Cloud Climatology Project (ISCCP), Documentation of cloud data. *WCRP* Report WMO/TD-No. 266, 122 pp. [Available from Dr. W. B. Rossow at NASA Goddard Space Flight Center, Institute for Space Studies, 2880 Broadway, New York, NY, 10025.]

Sassen, K., 1981: Infrared (10.6 μm) scattering and extinction in laboratory water and ice clouds. *Appl. Opt.*, **20**, 185–193.

——, C. J. Grund, J. Spinhirne, M. Hardesty and J. M. Alvarez, 1990: The 27–28 October 1986 FIRE IFO cirrus case study: a five lidar view of cirrus cloud structure and evaluation. *Mon. Wea. Rev.*, **118**, 2288–2312.

Shenk, W. E., and R. J. Curran, 1973: A multispectral method for estimating cirrus cloud top heights. *J. Appl. Meteor.*, **12**, 1213–1216.

Schiffer, R. A., and W. B. Rossow, 1983: The International Satellite Cloud Climatology Project (ISCCP): the first project of the World Climate Research Progamme. *Bull. Amer. Meteor. Soc.*, **64**, 779–784.

Spinhirne, J. D., D. L. Hlavka and W. D. Hart, 1988: ER-2 lidar observations from the October 1986 FIRE cirrus experiment. NASA TM 100704, 49 pp. [NTIS-N89-21444.]

Starr, D. O'C., 1987: A cirrus-cloud experiment: intensive field observations planned for FIRE. *Bull. Amer. Meteor. Soc.*, **68**, 119–124.

Stephens, G. L., 1980: Radiative properties of cirrus clouds in the infrared region. *J. Atmos. Sci.*, **37**, 435–446.

Stuhlmann, R., P. Minnis and G. L. Smith, 1985: Cloud bidirectional reflectance functions: a comparison of experimental and theoretical results. *Appl. Opt.*, **24**, 396–401.

Suttles, J. T., R. N. Green, P. Minnis, G. L. Smith, W. F. Staylor, B. A. Wielicki, I. J. Walker, D. F. Young, V. R. Taylor and L. L. Stowe, 1988: Angular radiation models for earth-atmosphere system: Volume I–Shortwave radiation. NASA RP 1184, 144 pp. [NTIS-N88-27677.]

Takano, Y., and K. N. Liou, 1989a: Radiative transfer in cirrus clouds: I. Single scattering and optical properties of oriented hexagonal ice crystals *J. Atmos. Sci.*, **46**, 3–20.

——, and ——, 1989b: Radiative transfer in cirrus clouds: II. Theory and computation of multiple scattering in an anisotropic medium. *J. Atmos. Sci.*, **46**, 21–38.

——, K. N. Liou and P. Minnis, 1989: Cirrus optical depth retrieval from satellite-measured bidirectional reflectance. *AMS Symp. on Role of Clouds in Atmos. Chem. and Global Climate*, Anaheim, CA, Amer. Meteor. Soc., 178–180.